Università degli Studi di Napoli Federico II

Dottorato di ricerca in FISICA

Ciclo: XXXIII

Coordinatore: Prof. Salvatore Capozziello

Full control of Josephson nonlinear processes in superconducting parametric devices for efficient control and readout of quantum circuits

Settore Scientifico Disciplinare: FIS/03

Candidato

Alessandro Miano

Tutori

Prof. Francesco Tafuri

Dott. Davide Massarotti

A.A. 2017/2020

Abstract

Parametric processes play a fundamental role in superconducting quantum information processing, as they provide a controllable tool for the elaboration of weak, coherent microwave tones down to the single-photon regime. These effects are in fact employed for many crucial applications, ranging from high-fidelity quantum limited readout of superconducting qubits to driving on-demand interactions between storage, processing and readout cavities in quantum processors. State-of-the-art superconducting devices that enable in-situ control of parametric processes are based on the Superconducting Nonlinear Asymmetric Inductive eLement (SNAIL), a superconducting loop threaded with an external magnetic flux that can be used to select the type of desired processes. However, with a single flux-tuning knob, the SNAIL Hamiltonian does not allow to independently choose the efficiency of a three or four-wave mixing process as well as the linear response. In order to obtain this type of freedom in Hamiltonian tailoring through superconducting circuits, in this thesis I propose a new device, the Gradiometric SNAIL (G-SNAIL), as a solution. A G-SNAIL implements an effective Hamiltonian that can be tuned in situ with two independent magnetic flux biases, thus providing an additional degree of freedom for the choice of the generated parametric processes. An experimental demonstration of such a feature is performed by employing a G-SNAIL as the elementary cell of a doubly flux-tunable parametric amplifier, capable to deliver a pure, Kerr-free three-wave mixing amplification at different operating frequencies. This device provides an experimental demonstration of the advanced Hamiltonian tuning capabilities that can be obtained with two flux-bias degrees of freedom, and is itself a very good candidate for delivering a noticeable progress in the field of synthesizing on-demand parametric processes.

Contents

Chapter 1

Main notions on superconducting circuits

Motivation

In the last 20 years, the field of superconducting quantum information processing has evolved very rapidly, and is currently growing even faster. The key feature for such a massive use of superconducting technologies for the practical implementation of quantum processors is basically the capability of synthesizing artificial atoms with superconducting microwave circuits [1, 2] that can be designed, simulated and characterized with very good precision. These circuits, namely qubits, are the carriers of binary quantum information, being two level systems operating at microwave frequency. In order to engineer interactions between multiple qubits, as well as reading their state in a quantum non-demolition manner, big efforts were made in the last 15 years to implement parametric processes between microwave photons and superconducting devices [3, 4] that can enhance the practical operability of the qubits. These energy-conserving processes are implemented in superconductivity by exploiting the nonlinear effects provided by Josephson junctions and are currently employed in many different applications. In fact, parametric processes play key roles in superconducting quantum circuits, ranging from delivering high fidelity, quantum-limited readout of qubits [5–10], to the control of interactions between the various cavities used to store, read and manipulate quantum information [11, 12]. Recently, many different approaches to have better capabilities of synthesizing on-demand parametric

processes have been proposed [8, 12–19]. Among these, the state-of-the-art solution relies on the Superconducting Nonlinear Asymmetric Inductive eLement (SNAIL) [20], a magnetic flux threaded superconducting loop that can be tuned in-situ in order to implement a desired combination of linear and nonlinear responses. The SNAIL has been employed to implement three-wave mixing (3WM) processes as well as four-wave mixing (4WM) ones, thanks to its enormous flexibility due to the ease in design and fabrication, as well as to the tuning via external magnetic flux. The most advanced Quantum Limited Amplifier (QLA) made with SNAILs is named the SNAIL Parametric Amplifier (SPA) [21, 22], where an array of 20 SNAILs is embedded in a microwave resonator to implement a 3WM resonant parametric amplifier. Despite its enormous success, the SNAIL tunability is still limited by the constraints of the Josephson effect, that strictly relates the nonlinear expansion coefficients with trigonometric relations. In this thesis work, a solution to this problem is proposed, employing a novel device called Gradiometric SNAIL (G-SNAIL). A G-SNAIL is a doubly flux-biased superconducting loop, whose potential energy function can be controlled by two independent external magnetic fluxes. This device is capable of delivering a combination of parametric processes that can be tuned in-situ by an additional degree of freedom with respect to the standard SNAIL. Its peculiarity allows to design tunable Hamiltonians with enhanced tuning of linear and nonlinear effects, for example, delivering Kerr-free 3WM amplification for different operating frequencies.

Here, the G-SNAIL is employed as the elementary cell of a doubly-flux tunable SPA, the Gradiometric SNAIL Parametric Amplifier (G-SPA), demonstrating the advanced Hamiltonian tailoring capabilities that can be obtained with two external bias knobs. In chapter 1, basics of superconducting quantum devices are presented, for both linear and nonlinear, Josephson junctions-based microwave circuits. In chapter 2, it is theoretically shown how single-flux biased superconducting loops can implement tunable Hamiltonians and their limits are explained. Then, the G-SNAIL is introduced and analyzed in order to demonstrate the advantages that its peculiar additional tuning degree of freedom can provide. This is particularly remarkable when G-SNAILs are used to build a G-SPA. In chapter 3, design, simulation and fabrication methods for a G-SPA are explained. In chapter 4 experimental data on the performances of the fabricated device are presented, analyzing its linear and nonlinear responses with a careful comparison with simulations based on the theoretical model presented in chapter 2. The ex-

periments confirmed that the additional tuning degree of freedom broadens the Hamiltonian-tailoring capability of superconducting circuits, demonstrating Kerr-free 3WM operations at different operating frequencies. Finally, in chapter 5, some applications and future directions are discussed.

1.1 Quantization of superconducting microwave circuits

Superconducting materials are well suited to be operated at microwave frequencies, as the superconducting gap of common materials as niobium or aluminum allows GHz range signals to be treated without breaking Cooper pairs and, consequently, preserving the superconducting behavior [23]. In this section, common microwave superconducting circuits will be introduced, with a focus on their quantum properties that allow to implement superconducting quantum devices as qubits and quantum-limited parametric amplifiers.

1.1.1 Harmonic LC oscillator

The simplest superconducting quantum circuit is composed by an inductor and a capacitor connected in parallel, namely an LC harmonic oscillator. With reference to figure 1.1, L is the inductance of the linear inductor and C is the capacitance of the capacitor. The node "a" is called *active node*, defined as a node where a purely inductive branch of the circuit meets a purely capacitive one. Active nodes are valuable tools for the design and analysis of superconducting quantum circuits. It is useful to introduce the active node flux ϕ_a, defined as [24]

$$\phi_a(t) = \int_{-\infty}^{t} V_a(\tau) d\tau = \Phi(t) \tag{1.1}$$

where V_a is the voltage between node a and ground in figure 1.1. Here, it is clear how the flux node coincides with the flux threaded into the inductor. The capacitor charge Q can also be related to ϕ_a by the relation

$$Q(t) = CV_a(t) = C\frac{d\phi_a(t)}{dt}. \tag{1.2}$$

From the last two equations, a natural choice is to elect ϕ_a as the coordinate of the system. As $\Phi = \phi_a$ and $Q = C\dot{\phi}_a$, this choice makes the potential energy

E_U of the circuit depend only on the inductor state and the kinetic energy E_K only on the capacitor state. This will have important consequences for the analysis of superconducting circuits, as any external magnetic field threaded with an inductive element will appear as a tunable parameter in the potential energy of the system. The total state of this LC oscillator can be described by means of the charge $C\dot{\phi}_a$ on one of the two plates of the capacitor and the magnetic flux ϕ_a threaded into the inductor. The energies stored into the two components can be expressed as

$$E_K(\dot{\phi}_a) = \frac{C\dot{\phi}_a^{\,2}}{2} \qquad\qquad E_U(\phi_a) = \frac{\phi_a^2}{2L}, \tag{1.3}$$

so the Lagrangian of the LC oscillator reads as follows

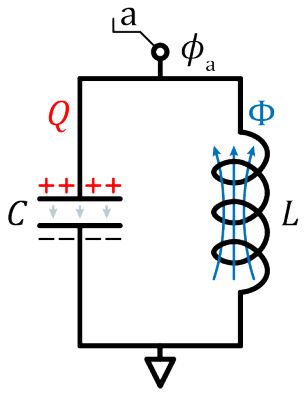

Figure 1.1: LC harmonic oscillator. The node where the capacitor and the inductor are connected is called "active node". An equivalent flux ϕ_a can be associated to this node.

$$\mathcal{L} = \frac{C\dot{\phi}_a^{\,2}}{2} - \frac{\phi_a^2}{2L} \tag{1.4}$$

and the equation of motion takes the form

$$\frac{d^2\phi_a}{dt^2} + \omega_0^2\phi_a = 0, \tag{1.5}$$

where $\omega_0 = 1/\sqrt{LC}$ is the characteristic frequency of the oscillator.

From the definition of conjugate momentum and the Lagrangian (1.4) derives that (ϕ_a, Q) are a set of canonical coordinates. The Hamiltonian of

the system is then derived from a Legendre transformation of Lagrangian (1.4) and reads

$$H = \frac{Q^2}{2C} + \frac{\phi_a^2}{2L}. \tag{1.6}$$

The quantization of the harmonic oscillator is then performed by promoting Q and ϕ_a to operators $\boldsymbol{Q}$ and $\boldsymbol{\phi_a}$, satisfying the commutation rule $[\boldsymbol{\phi_a}, \boldsymbol{Q}] = i\hbar$. It is useful to introduce charge number operator $\boldsymbol{N} = \boldsymbol{Q}/2e$ and phase operator $\boldsymbol{\varphi} = 2\pi\boldsymbol{\phi_a}/\Phi_0$, so that the quantized Hamiltonian reads as

$$\boldsymbol{H} = 4E_C\boldsymbol{N}^2 + E_L\boldsymbol{\varphi}^2. \tag{1.7}$$

Here, $E_C = e^2/2C$ is the energy contribution from the capacitor, $E_L = (\Phi_0/2\pi)^2/L$ is the contribution from the inductor of the LC oscillator and $\Phi_0 = h/2e$ is the magnetic flux quantum. It is further possible to introduce the creation and annihilation operators $\boldsymbol{a}^\dagger$ and $\boldsymbol{a}$

$$\begin{aligned} \boldsymbol{\varphi} &= \varphi_{\mathrm{ZPF}}(\boldsymbol{a} + \boldsymbol{a}^\dagger) \\ \boldsymbol{N} &= \frac{1}{i} n_{\mathrm{ZPF}}(\boldsymbol{a} - \boldsymbol{a}^\dagger) \end{aligned} \tag{1.8}$$

where φ_{ZPF} and N_{ZPF} are the zero-point fluctuations of phase and number operators, expressed as

$$\begin{aligned} \varphi_{\mathrm{ZPF}} &= \frac{2\pi}{\Phi_0}\sqrt{\frac{\hbar Z_0}{2}} \\ N_{\mathrm{ZPF}} &= \frac{1}{2e}\sqrt{\frac{\hbar}{2Z_0}} \end{aligned} \tag{1.9}$$

where $Z_0 = \sqrt{L/C}$ is the intrinsic impedance of the LC resonator. With this further step, the harmonic oscillator Hamiltonian acquires the well known form

$$\boldsymbol{H} = \hbar\omega\left(\boldsymbol{a}^\dagger\boldsymbol{a} + \frac{1}{2}\right). \tag{1.10}$$

1.1.2 Josephson junctions and nonlinear elements

The most important electronic component in superconducting quantum information processing is the Josephson tunnel Junction (JJ). A JJ is obtained

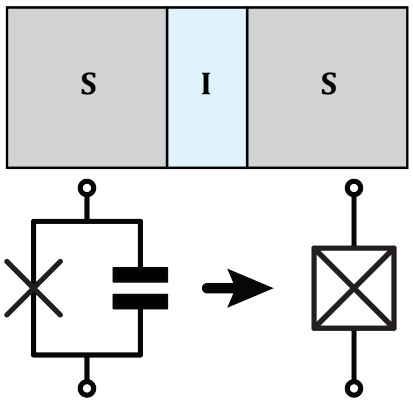

Figure 1.2: Josephson tunnel junction. Two superconducting electrodes are separated by a thin oxide that forms a tunnel barrier and a parallel capacitance. The schematic represents both tunneling and capacitive contributes to the conduction.

when two superconducting electrodes are separated by a thin insulating oxide [25,26] that Cooper pairs can tunnel through, forming a Superconductor-Insulator-Superconductor (SIS) junction, as in figure 1.2. Given the phases φ_1 and φ_2 of the two superconducting electrodes, the phase drop across the junction is $\varphi = \varphi_2 - \varphi_1$, and the transport properties of the JJ are defined by the following Josephson equations [25]

$$\begin{aligned} I(\varphi) &= I_c \sin\varphi \\ V &= \frac{\Phi_0}{2\pi}\frac{d\varphi}{dt} \end{aligned} \tag{1.11}$$

where I_c is the critical current of the JJ, defined as the maximum current that can flow through it without breaking the superconductivity and V is the voltage drop across the JJ. The physical structure of a JJ results also in a capacitive contribution to the transport, to be considered in parallel with the tunneling one. The overall schematic of a JJ is a cross inside a box (see figure 1.2), representing both tunneling and capacitive contributes to the transport.

Being a nonlinear element, a JJ can implement many features that are not possible in bare superconducting metals. This is particularly useful, for example, to provide the required anharmonicity for fabricating practical qubits or, more in general, superconducting nonlinear circuits. These can be designed to simulate Hamiltonians that can implement various operations such as 3WM or 4WM processes.

Usually, Josephson junctions are embedded in more complex inductive nets, where also linear inductors are present. To describe a purely inductive circuit, made by JJs and linear inductors, it is helpful to compute its equivalent nonlinear inductance. By keeping the same choice of the previous paragraph, where the phase across an inductance is elected as coordinate, the energetic contribute of a nonlinear inductance with a phase drop φ has to be considered a pure potential energy $U(\varphi)$. For a physical system, the internal energy can be computed as

$$E = \int v_{\mathrm{i}} dv_{\mathrm{e}} \tag{1.12}$$

where v_{i} and v_{e} are, respectively, intensive and extensive variables that describe the system. In figure 1.3 a generic two terminal element (will be called a *dipole* in the rest of the manuscript) is represented, characterized by a current-phase relation $I(\varphi)$. If it gets split in two identical sub-dipoles along the current-flow line, the phase drop halves while the current remains the same for each of the two. As a consequence, in this picture, the phase φ behaves as an extensive variable, while current I is the intensive one. Having classified the two variables, with reference to the equation (1.12), the potential energy of a purely inductive, generic dipole is computed as

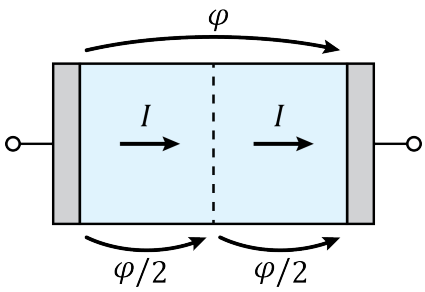

Figure 1.3: Intensive and extensive variables in a 1D inductive dipole implementing an $I(\varphi)$ relation in the light blue region. If a cut along the current flow line is made in the middle of the dipole, the phase drop across the two resulting sections is halved, while the current remains the same. Thus, in this picture, the phase represents the extensive variable while the current the intensive one.

$$U(\varphi) = \frac{\Phi_0}{2\pi} \int I(\varphi) d\varphi. \tag{1.13}$$

A first understanding comes from this expression: the minima of the potential energy $U(\varphi)$ of an inductive dipole correspond to zeroes of the current flowing through it. In fact, a phase value φ_0 that minimizes $U(\varphi)$ is solution of the equation

$$\frac{2\pi}{\Phi_0}\frac{dU}{d\varphi}(\varphi_0) = I(\varphi_0) = 0 \tag{1.14}$$

Moreover, as the differential inductance of a nonlinear element is defined as $d\phi/di$, and considering that $\phi = (\Phi_0/2\pi)\varphi$, the inductance of a generic dipole is related to its potential energy by the relation

$$L(\varphi) = \left(\frac{2\pi}{\Phi_0}\right)^2 \frac{1}{\dfrac{d^2U}{d\varphi^2}}. \tag{1.15}$$

This last expression is particularly useful when describing complex dipoles whose effective inductance cannot be retrieved without considering the nonlinear effects of JJs.

1.2 Superconducting qubits

Quantum computing is based on the processing of quantum information encoded in abstract entities known as qubits. A qubit is a quantum system that lives in a two-dimensional Hilbert space. Its state can then be described as

$$|\psi\rangle = \alpha\,|0\rangle + \beta\,|1\rangle \tag{1.16}$$

where α and β are complex coefficients, satisfying the relation $|\alpha|^2 + |\beta|^2 = 1$ and the eigenstates of the qubit $|0\rangle$ and $|1\rangle$ represent the possible outcomes of an ideal measurement on the system. As $|\alpha|$ and $|\beta|$ are constrained by a pitagorean relation, and the measurement of a wavefunction is independent from any global phase, it is possible to define an angle θ and a phase ϕ such that the wavefunction (1.16) can be expressed as

$$|\psi\rangle = \cos\left(\frac{\theta}{2}\right)|0\rangle + e^{i\phi}\sin\left(\frac{\theta}{2}\right)|1\rangle \tag{1.17}$$

Then, being described by two variables, the wavefunction $|\psi\rangle$ lives on the surface of a 2-D manifold, namely the Block sphere, where all the possible superpositions of the eigenstates $|0\rangle$ and $|1\rangle$ are represented as a function of

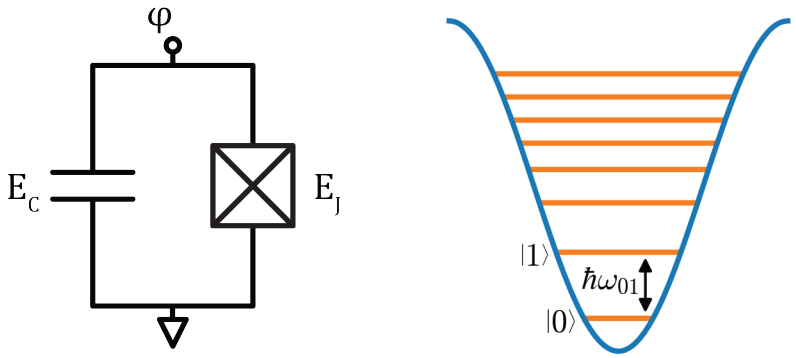

Figure 1.4: Transmon qubit. Shunting a Josephson junction with a large capacitance such that $E_J/E_C \approx 50$ makes the device very resilient to charge noise and, at the same time, keeps enough anharmonicity such that is possible to isolate the $0 \rightarrow 1$ transition of the circuit and employ the first two energy levels of the transmon as a qubit.

θ and ϕ. In practice, a qubit can be implemented by any two-level system present in nature, for example photon polarization, or an artificial one, as a superconducting anharmonic oscillator. Usually, artificial two-level systems are extracted from a much richer energy level structure, where the ground level and the first excited one are elected as $|0\rangle$ and $|1\rangle$ states, representing the eigenstates of a qubit. It is then important to be able to separate these two levels from all the others, in order to avoid unwanted transitions of the physical system that can push it out from the two-dimensional subspace where it is operated as a qubit. Such a separation can be obtained at hardware level, for example, when a qubit is implemented by using the first two levels of a nonlinear resonator. In fact, the anharmonicity makes possible to isolate two contiguous level whose population can be controlled with a resonant coherent drive that won't interact with any other possible transition of the system. The state-of-the-art qubits are based on the transmon circuit [1, 2], represented in figure 1.4 on the left. Thanks to the presence of a nonlinear inductance implemented by a Josephson junction, the energy levels of a transmon are not equally spaced (see right panel of figure 1.4) as in an harmonic oscillator. As a consequence, the first two levels of the transmon can be employed as $|0\rangle$ and $|1\rangle$ eigenstates of a qubit, resonating at a frequency ω_{01} as in the right panel of figure 1.4. Derived from the Cooper

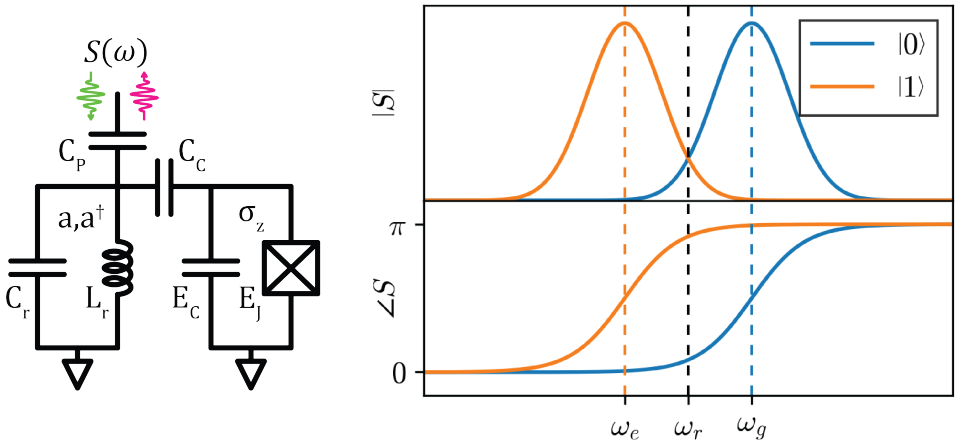

Figure 1.5: Dispersive coupling between a linear resonator and a transmon qubit. If transition frequency of a qubit and resonance frequency of a cavity are detuned, these can be dispersively coupled in such a way that the resonance frequency of the linear resonator is "dressed" by the state of the qubit, but not in resonance with its transition. This allows an indirect, quantum non demolition measurement of the qubit state by probing the resonance frequency of the dressed resonator, whose amplitude and phase responses depend on the two-level system.

pair box [27], the transmon is characterized by the Hamiltonian

$$\mathbf{H} = 4E_C\mathbf{N}^2 - E_J\cos\boldsymbol{\varphi} \tag{1.18}$$

and operates in an intermediate regime where charge energy $E_C = e^2/2C$ is much smaller than Josephson energy $E_J = \Phi_0 I_c/2\pi$. This makes the circuit very resilient to charge noise, as the charge dispersion of the energy levels of Hamiltonian (1.18) is proportional to $\exp\left(-\sqrt{8E_J/E_C}\right)$ [1, 2]. On the other hand, the relative anharmonicity of the transmon $\alpha_r = (\omega_{12} - \omega_{01})/\omega_{01}$ decreases with a power law in E_J/E_C [1, 2] instead than exponentially as charge dispersion. Here, ω_{mn} is the resonance frequency corresponding to a transition between levels m and n. The ratio E_J/E_C is usually 50 or more for a transmon, balancing charge noise robustness and anharmonicity. The state of a transmon can be experimentally measured, for example, by coupling it to a bus resonator that is far detuned from the $|0\rangle \rightarrow |1\rangle$ transition of the qubit. This type of coupling is called "dispersive coupling", and can be obtained with a circuit schematic as in the left panel of figure 1.5. Here,

the bus resonator is made with linear inductance L_r and a capacitance C_r, corresponding to a bare resonance frequency $\omega_r = 1/\sqrt{L_r C_r}$, and it is coupled to a transmon qubit via the coupling capacitor C_C. The state of the bus resonator is described in terms of $\mathbf{a}$ and $\mathbf{a}^\dagger$ operators, while the state of the transmon qubit is described by the σ_z Pauli operator. After some manipulations [3], the Hamiltonian of the circuit reads as follows

$$\mathbf{H} = \hbar \left(\omega_r + \frac{g^2}{\Delta} \sigma^z \right) \mathbf{a}^\dagger \mathbf{a} + \frac{\hbar}{2} \left(\Omega + \frac{g^2}{\Delta} \right) \sigma^z, \tag{1.19}$$

where g is the coupling strength between the transmon qubit and the resonator, mainly depending on capacitance C_C, Ω is the vacuum Rabi oscillation frequency of the qubit and $\Delta = \Omega - \omega_r$ is the qubit-resonator detuning. From Hamiltonian (1.19) it arises that the resonance frequency of the bare resonator ω_r is shifted by the qubit by a factor $\pm g^2/2\Delta$, depending on state of the qubit. Thus, when probing the reflection coefficient $S(\omega)$ of the circuit in figure 1.5, the response (right panel of the same figure) will show a resonance at $\omega_g = \omega_r + g^2/2\Delta$ if the qubit collapsed in the $|0\rangle$ state, or at $\omega_e = \omega_r - g^2/2\Delta$ if the qubit collapsed in the $|1\rangle$ state at the time of the measurement. Then, by measuring the frequency response of the resonator at a particular frequency, where either phase or amplitude response is highly sensitive to the qubit state, it is possible to know the eigenstate in which the qubit collapsed at the time of the measurement. Being this an indirect measurement of the σ^z operator, and because σ^z commutes with the Hamiltonian of the system (1.19), this interaction represents a quantum non-demolition measurement of the two-level system [3, 4]. For such a measurement to be effective, it is required that the energy levels of the circuit are not populated by thermal photons. This is ensured as superconducting quantum circuits are operated on the 20 mK stage of a dilution refrigerator, corresponding to a thermal energy of about 2.8×10^{-25} J, capable of exciting transitions in the order of 400 MHz. As qubits and resonators frequencies are usually > 4 GHz, the 20 mK temperature is low enough to not affect the correct operation of the devices. Moreover, it is important to highlight that the resonator should be probed with weak microwave coherent signals, corresponding to an average photon number $\bar{n} \approx 1$, in order to not excite unwanted transitions of the qubit. This poses the problem of how to detect such weak microwave tones with an high Signal to Noise Ratio (SNR), in order to implement an high fidelity readout that is not disturbed by noise. An answer to this question comes with the introduction of QLAs [7, 10, 28] that can detect and amplify

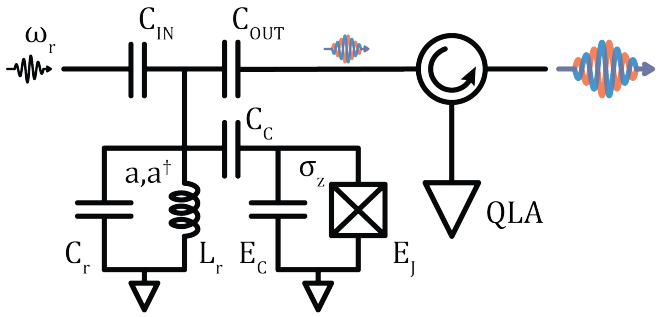

Figure 1.6: Simplified schematic for the dispersive readout of a transmon qubit. A weak, coherent microwave tone is sent to the resonator at its characteristic frequency $\omega_r = 1\sqrt{L_r C_r}$. The pulse gets reflected by the resonator, with a phase that depends on the measured value of σ_z operator of the qubit, thus encoding the result of a projective measurement of the qubit state. The ouput pulse is then amplified with a Quantum Limited Amplifier (QLA), in this case operated in reflection, in order to increase the readout fidelity.

single photon coherent signals, preserving information on both their amplitude and phase, with the least minimum amount of added noise predicted by quantum mechanics (corresponding to half photon). These amplifiers rely on nonlinear parametric processes provided by Josephson junctions based circuits, properly engineered to work as three-wave mixers or four-wave mixers. QLAs can be operated, for example, as in figure 1.6, where a QLA operated in reflection amplifies coherently the pulse reflected by a resonator that is dispersively coupled to a qubit, increasing the readout fidelity.

Another possible way to implement superconducting qubits uses the idea of building high-Q linear microwave cavities with superconducting materials, for example aluminum, and employ their lower energy levels in order to encode quantum information or a superposition of coherent states [29]. In this case, as absorption and emission spectra are degenerate as in any harmonic oscillator, a transmon is coupled to the 3D cavity in order to distinguish the occupied state at the time of readout. With these 3D cavities it is possible to build very clean quantum systems that can implement complex algorithms with very high fidelity. A key ingredient for this operations is the capability of driving on-demand interactions between multiple cavities, again using properly engineered parametric processes. For example given two cavities A and B (see figure 1.7), each one encoding a two-level-system

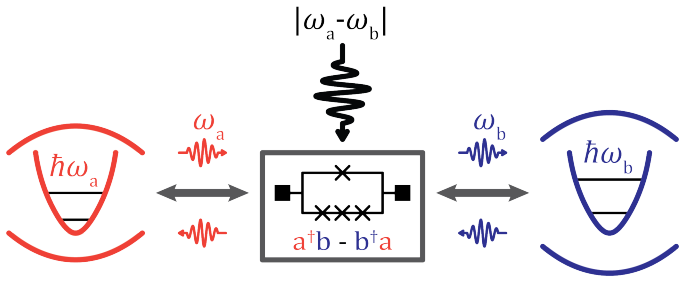

Figure 1.7: Engineering beam-splitter interaction between two superconducting cavities at different operating frequencies. Cavities A and B are coupled to a non-linear device (a SNAIL in the figure), capable of three-wave mixing operations. When pumped with a microwave signal, oscillating at a frequency $|\omega_a - \omega_b|$, the device can implement an effective beam-splitter interaction that mediates the exchange of a single photon between the two cavities.

with its ground and first excited state, it is possible to mediate a coherent photon exchange between them. Such an exchange can take place if the two cavities interact via a beam-splitter Hamiltonian of the type

$$H_{BS} = \boldsymbol{a}^\dagger \boldsymbol{b} - \boldsymbol{b}^\dagger \boldsymbol{a} \tag{1.20}$$

where $\boldsymbol{a}$ and $\boldsymbol{b}$ are annihilation operators referring to cavities A and B, respectively. The interaction (1.20) can be engineered with a superconducting dipole capable of 3WM parametric processes, for example a SNAIL [20]. When such a dipole is coupled to both cavities, as in figure 1.7, it can be pumped with a microwave tone oscillating at a frequency $\omega_p = |\omega_a - \omega_b|$, where ω_a and ω_b are the transition frequencies of the two-level-systems encoded in cavities A and B, respectively. In this way, the total Hamiltonian of the system reads

$$H = \hbar\omega_a \boldsymbol{a}^\dagger \boldsymbol{a} + \hbar\omega_b \boldsymbol{b}^\dagger \boldsymbol{b} + g(\boldsymbol{a}^\dagger \boldsymbol{b} - \boldsymbol{b}^\dagger \boldsymbol{a}) \tag{1.21}$$

where g is a coupling factor that depends, in general, by the coupling between the 3WM dipole (supposed identically coupled to both cavities for simplicity) and the strength of the pumping tone at frequency $|\omega_a - \omega_b|$. Hamiltonian (1.21) describes a dynamic where, if for example cavity A is excited with one resonant photon and the cavity B is in the vacuum state, with a coupling $g \neq 0$ the photon in cavity A can be destroyed and, consequently, a photon in

cavity B is created. This mechanism applies as well if a photon in cavity B, supposed excited, need to be transferred in cavity A, supposed in the vacuum state. This is just another, among many, of the applications that parametric processes enable in superconducting quantum information processing.

Chapter 2

Superconducting parametric circuits

2.1 Parametric processes with superconducting circuits

Parametric processes are light-matter interactions where the material's quantum state remains unchanged. As a result, coherent electromagnetic signals can be elaborated by these processes without any induced decoherence. This peculiarity made them lead actors in quantum information processing, where they are employed to implement many important functions as coupling between cavities, quantum limited amplification, entanglement and so on.

First introduced in nonlinear optics [30], parametric processes have been enabled also on superconducting platforms at microwave frequencies [7, 31–33], with particular applications in near-quantum-limited amplification [5, 6, 8, 9, 13, 15, 17, 20, 34–36]. This breakthrough has been possible thanks to Josephson tunnel junctions, whose tunable flux-current relation can implement different combinations of linear and nonlinear effects with a very precise control provided by external applied fields. In fact, a superconducting loop embedding multiple JJs and threaded by an external static magnetic flux Φ_e (see figure 2.1) operating at GHz frequency can be described by the relation

$$\Phi_{\mu w}(t) = \sum_n a_n(\Phi_e) I^n_{\mu w}(t) \tag{2.1}$$

where $I_{\mu w}$ and $\Phi_{\mu w}$ are microwave perturbations of the current and equiv-

alent flux of the the dipole, respectively. Relation (2.1) clearly shows how

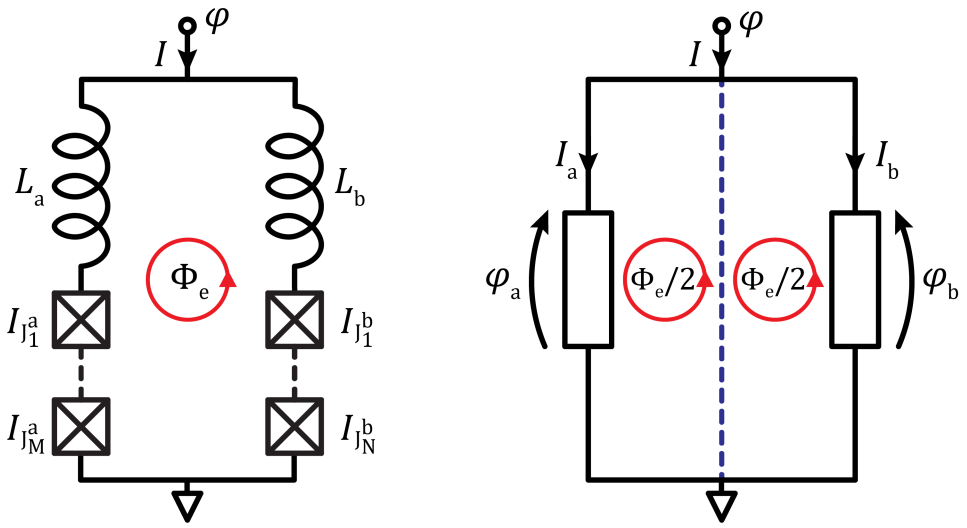

Figure 2.1: Superconducting loop with two inductive branches a and b, and threaded by an external magnetic flux Φ_e. Each branch is itself a dipole characterized by an $I_s(\varphi_s)$ relation.

Josephson based circuits are capable to implement nonlinear optics effects at GHz frequencies, mimicking the optical response of a nonlinear media

$$p(t) = \sum_n \chi_n E^n(t) \tag{2.2}$$

where p is the electric polarization density, E is the electric field and χ_n are susceptibility tensors that characterize the media. In expression (2.1), the microwave susceptibilities $a_n(\Phi_e)$ are variable coefficients that can be flux-tuned to select the desired nonlinear effects and, in general, depend on the overall design of the circuit. It is possible to design such a circuit in order to have a predominant three-wave mixing term $a_2(\bar{\Phi}_e)$ or four-wave

mixing term $a_3(\bar{\Phi}_e)$ when flux biased in a sweet spot $\bar{\Phi}_e$. Moreover, its linear response $a_1(\bar{\Phi}_e)$ can be designed to match a required value in order to fulfill specifications regarding impedance matching or resonance frequency of a parent device. From all these considerations, it is quite clear how powerful this approach is: by properly engineering a flux-biased superconducting loop, it is possible to synthesize a generic nonlinear media at microwave frequencies providing the desired response for a given application. In order to represent the behavior of the circuit on the left side of figure 2.1, one would first write the total potential energy of each branch as a sum of the energies of the individual components

$$U_s(\varphi_s) = \left(\frac{\Phi_0}{2\pi}\right)^2 \frac{\varphi_{L_s}^2(\varphi_s)}{2L_s} - \sum_{n=1}^{N_s} E_{J_n^s} \cos\varphi_n^s(\varphi_s) \tag{2.3}$$

where linear inductor fluxes φ_{L_s} and phase differences across the junctions φ_n^s on branch s can be expressed as a function of the branch flux φ_s only. Unfortunately, it is not always possible to find analytical expressions for $\varphi_{L_s}(\varphi_s)$ and $\varphi_n^s(\varphi_s)$, as these are in general solutions of the nonlinear algebraic system

$$\begin{cases} \varphi_{L_s}(\varphi_s) + \sum_{n=1}^{N_s} \varphi_n^s(\varphi_s) = \varphi_s \\ \varphi_{L_s}(\varphi_s) - \beta_1^s \sin\varphi_1^s(\varphi_s) = 0 \\ \qquad\vdots \\ \varphi_{L_s}(\varphi_s) - \beta_{N_s}^s \sin\varphi_{N_s}^s(\varphi_s) = 0 \end{cases} \tag{2.4}$$

where $\beta_n^s = 2\pi L_s I_{J_n^s}/\Phi_0$. First equation of system (2.4) relates the branch phase to the phases across the individual components and the remaining N_s equations state that the current is the same in each component of the branch. In total, these N_s+1 equations allow to express all the N_s+1 phases across the elements in branch s as a function of φ_s only, thus providing a more accessible expression for the branch potential energy. For numerical computation, it might be easier to obtain the branch potential energy as

$$U_s(\varphi_s) = \frac{\Phi_0}{2\pi} \int I_s(\varphi_s) d\varphi_s \tag{2.5}$$

when one expresses the branch current as

$$I_s(\varphi_s) = \frac{\Phi_0}{2\pi} \frac{\varphi_{L_s}(\varphi_s)}{L_s}. \tag{2.6}$$

Once an expression for each branch potential energy has been found, and keeping in mind phase conservation equations arising from the circuit schematic in the right panel of figure 2.1

$$\begin{aligned} \varphi_a &= \varphi + \frac{\varphi_e}{2} \\ \varphi_b &= \varphi - \frac{\varphi_e}{2} \end{aligned} \tag{2.7}$$

where $\varphi_e = 2\pi\frac{\Phi_e}{\Phi_0}$, the total potential energy of the flux-threaded superconducting loop reads as follows

$$U(\varphi) = U_a\left(\varphi + \frac{\varphi_e}{2}\right) + U_b\left(\varphi - \frac{\varphi_e}{2}\right). \tag{2.8}$$

It is then possible to find an operating point φ_0 for the superconducting loop such that

$$\frac{2\pi}{\varphi_0}\left.\frac{dU}{d\varphi}\right|_{\varphi_0} = I_a\left(\varphi_0 + \frac{\varphi_e}{2}\right) + I_b\left(\varphi_0 - \frac{\varphi_e}{2}\right) = 0. \tag{2.9}$$

In general, equation (2.9) admits more than one solution, and there are precise design criteria in order to have a single or multiple minima potential. Once an operating point has been selected, one can finally expand the potential as

$$U(\varphi) = \sum_{n=2}^{\infty} \frac{c_n(\varphi_e)}{n!}(\varphi - \varphi_0)^n \tag{2.10}$$

where φ_0 is the equilibrium point of the system around which the potential energy has been expanded, and is in general a function of Φ_e. Note that Taylor expansion (2.10) starts from $n = 2$, as the offset c_0 doesn't contribute to the device dynamics and $c_1 = (dU/d\varphi)\,|\varphi_0 = 0$ as of equation (2.9). Inserting such a tunable nonlinear inductance in an LC resonator as in figure 2.2 the following Hamiltonian, expanded up to the fourth order, builds up

$$H = 4E_C\mathbf{N}^2 + \frac{c_2(\varphi_e)}{2!}\boldsymbol{\varphi}^2 + \frac{c_3(\varphi_e)}{3!}\boldsymbol{\varphi}^3 + \frac{c_4(\varphi_e)}{4!}\boldsymbol{\varphi}^4 + \dots \tag{2.11}$$

where $c_n(\varphi_e)$ are expansion coefficients of the resonator potential energy (2.10), $\boldsymbol{N}$ and $\boldsymbol{\varphi}$ are the operators defined in the first chapter. Introducing creation and annihilation operators $\boldsymbol{a}^\dagger$ and $\boldsymbol{a}$ as for harmonic oscillators, the Hamiltonian (2.11) acquires the following form

$$H = \hbar\omega(\varphi_e)\boldsymbol{a}^\dagger\boldsymbol{a} + g_3(\varphi_e)(\boldsymbol{a} + \boldsymbol{a}^\dagger)^3 + g_4(\varphi_e)(\boldsymbol{a} + \boldsymbol{a}^\dagger)^4 + \dots \tag{2.12}$$

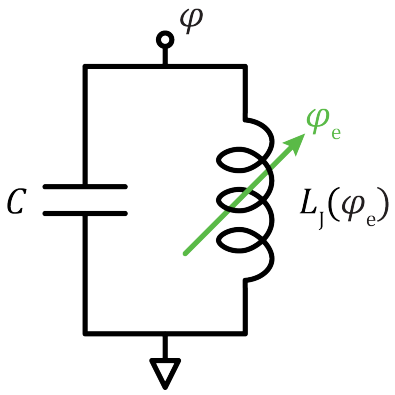

Figure 2.2: Tunable nonlinear LC resonator. A purely inductive nonlinear superconducting loop threaded by an external phase bias φ_e is shunted by a capacitance C, providing a kinetic component to implement a nonlinear oscillator.

where

$$\begin{aligned} \omega(\varphi_e) &= \sqrt{\frac{c_2(\varphi_e)}{C}} \\ g_3(\varphi_e) &= \frac{c_3(\varphi_e)}{2c_2(\varphi_e)}\sqrt{\frac{\omega(\varphi_e)E_C}{\hbar}} \\ g_4(\varphi_e) &= \frac{c_4(\varphi_e)}{c_2(\varphi_e)}E_C \end{aligned} \tag{2.13}$$

C being the capacitance of the resonator.

In the Hamiltonian (2.12), coefficient $g_3(\varphi_e)$ enables a trilinear term of the type $\mathbf{a^2a^\dagger}$, coming from the expansion of $(\boldsymbol{a}+\boldsymbol{a}^\dagger)^3$. Such a term can provide three-wave mixing operation when, for example, $\boldsymbol{a} = \boldsymbol{s}+\boldsymbol{i}+\alpha_p e^{i\omega_p t}\boldsymbol{I}$, where $\boldsymbol{s}$ and $\boldsymbol{i}$ are annihilation operators referring to signal and idler tones, respectively, and $\alpha_p e^{i\omega_p t}\boldsymbol{I}$ represents a strong, classical pump tone with amplitude α_p and frequency ω_p. Moreover, the coefficient $g_4(\varphi_e)$ can provide four-wave mixing behavior as well as other terms that can be poisonous if a pure three-wave mixing is desired. Among these, Kerr effect [21, 22, 37] is one of the most critical to deal with, as it strongly affects the performances of superconducting three-wave mixing circuits in many applications. Kerr mainly arises from the term $(\boldsymbol{a}+\boldsymbol{a}^\dagger)^4$ of the Hamiltonian (2.11), containing operators of the type $(\mathbf{a}^\dagger\mathbf{a})^2$ that can provide a photon number dependence of the resonance frequency ω of a nonlinear LC oscillator. In the following

section, the main 3WM-ready superconducting loops capable of Kerr-free operations will be described, namely the rf-SQUID and the SNAIL.

2.1.1 Three-wave mixing in superconductivity

As introduced in the last section, three-wave mixing processes can be calibrated in superconducting nonlinear loops when they implement a third order nonlinearity c_3 in an effective potential energy $U(\varphi)$. A first example of this comes from the flux-threaded rf-SQUID (figure 2.3) that implements the potential energy

$$\frac{U(\varphi)}{E_L} = \frac{1}{2}\varphi^2 - \beta\cos\left(\varphi - \varphi_e\right) \tag{2.14}$$

where the condition $\beta = E_J/E_L < 1$ needs to be satisfied in order to have a

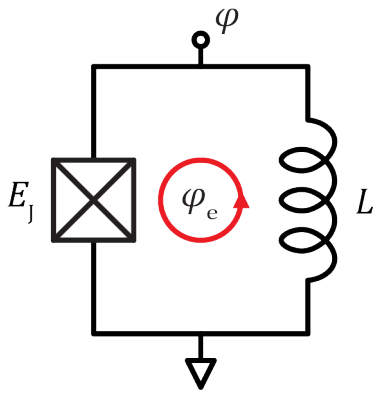

Figure 2.3: Flux-threaded rf-SQUID. A Josephson junction with energy E_J is shunted by a linear inductance L and the resulting loop is threaded by an external magnetic flux.

single-minimum potential energy function for each value of φ_e. The usefulness of an external flux is immediately clear once one notices that, for $\varphi_e = 0$, the function (2.14) admits the minimum $\varphi_0 = 0$ and the three-wave mixing coefficient $c_3 = 0$ in its proximity. For this reason, the only way to tune up three-wave mixing is to control the operation of an rf-SQUID by the application of an external flux. On this basis, a three-wave mixing traveling wave parametric amplifier was proposed and implemented by Zorin et al. [14, 15], confirming the operability of rf-SQUIDs for 3WM. It is worth noticing that,

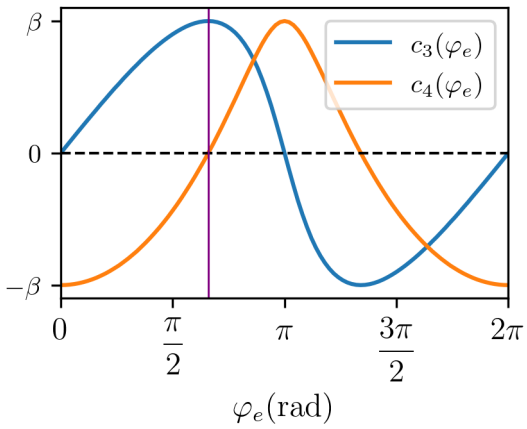

Figure 2.4: Third and fourth order expansion coefficients as a function of external flux φ_e for the potential energy of an rf-SQUID. Because there is only one tunable inductive branch, an rf-SQUID always offers maximum c_3 when $c_4 = 0$ (purple line).

because the rf-SQUID has only one tunable inductive branch (the contribution of linear inductor does not vary with external flux), coefficients c_3 and c_4 are only provided by the expansion of the same $\cos(\varphi - \varphi_e)$ term in the function (2.14), thus when one has maximum magnitude the other is zero, and vice-versa. Provided that φ_0 is an operating point, the coefficients are expressed as

$$\begin{aligned} c_3 &= -\beta \sin\left[\varphi_0(\varphi_e) - \varphi_e\right] \\ c_4 &= -\beta \cos\left[\varphi_0(\varphi_e) - \varphi_e\right] \end{aligned} \tag{2.15}$$

and the trigonometric relation $c_3^2 + c_4^2 = \beta^2$ holds. These coefficients are plotted as a function of φ_e in figure 2.4 where it is clear how, when c_3 is maximum, c_4 is suppressed and viceversa. Another superconducting loop that was recently used for 3WM operations in superconducting quantum information processing is the Superconducting NonLinear Asymmetric Inductive Element (SNAIL) [20–22], where the linear branch of the rf-SQUID is replaced by an array of 3 Josephson junctions (purple JJs in figure 2.5) with energy E_J, while the small junction (in black) has an energy αE_J where $\alpha \leq 0.3$ to implement a single-minumum potential energy. A SNAIL implements the

potential energy

$$\frac{U(\varphi)}{E_J} = -3\cos\frac{\varphi}{3} - \alpha\cos\left(\varphi - \varphi_e\right) \tag{2.16}$$

where the linear term is substituted with a weakly nonlinear one. This term can now contribute to the nonlinear expansion coefficients as a function of external magnetic flux φ_e. Such a configuration extends the possible choices

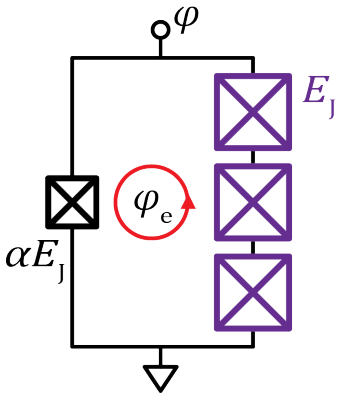

Figure 2.5: SNAIL tunable inductive loop. A small JJ is shunted with an array of three bigger JJs. The ratio between the Josephson energy of the small JJ and each of the big JJs is α.

of c_3 and c_4 coefficients because of the presence of tunable inductances in both branches of the loop. In fact, for a SNAIL, these coefficients are given by

$$\begin{aligned} c_3 &= -\frac{\sin\left[\dfrac{\varphi_0(\varphi_e)}{3}\right]}{9} - \alpha\sin\left[\varphi_0(\varphi_e) - \varphi_e\right] \\ c_4 &= -\frac{\cos\left[\dfrac{\varphi_0(\varphi_e)}{3}\right]}{27} - \alpha\cos\left[\varphi_0(\varphi_e) - \varphi_e\right] \end{aligned} \tag{2.17}$$

so is possible to choose α if a given combination of c_3 and c_4 is required for the desired behavior of the circuit. In figure 2.6 it is shown how, with a SNAIL, $c_4 \neq 0$ when c_3 is maximized, a feature not available with an rf-SQUID. With a SNAIL, is easy to implement the required value for the design parameter α, since the Josephson junction energy can be tuned with higher precision than the linear inductance of a wire. This advantage directly comes from

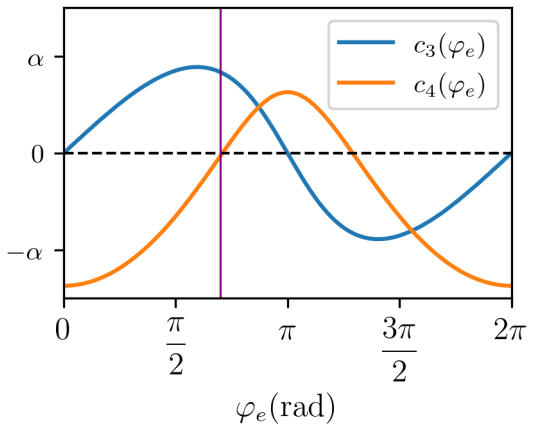

Figure 2.6: Nonlinear expansion coefficients for a SNAIL. The presence of two nonlinear branches allows to tune the relation between c_3 and c_4 in order to mix their values without the typical contraint of an rf-SQUID.

the fact that JJs offer a purely kinetic inductance, thus there is no magnetic field involved into the inductive behavior. In fact, the inductance of a wire inductor strongly depends on how the magnetic field lines interact with the surrounding environment, and could require non-trivial magnetic simulations to be extracted with high accuracy. This is even more true in superconducting materials, where Meissner effect needs to be taken into account to compute a realistic profile of the magnetic field. These peculiarities made the SNAIL a perfect candidate to implement the first Kerr-free three-wave mixing dipole that currently represents the state-of-the-art element for parametric processes with superconducting circuits [20]. For example, most of the resonant 3WM quantum-limited parametric amplifiers are made with SNAILs [21, 22, 37] and, recently, the functionality of a 4WM TWPA based on SNAILs with unprecedented performances has been demonstrated [35].

Despite their wide operability, rf-SQUIDs and SNAILs suffer from a tunability constraint that arises from the trigonometric nature of the Josephson effect. In fact, both potential energies (2.14) and (2.16) have their flux-tunability embedded in the $\cos(\varphi - \varphi_e)$ term that, if expanded with trivial trigonometric relations, becomes

$$\cos(\varphi - \varphi_e) = \cos\varphi_e \cos\varphi + \sin\varphi_e \sin\varphi. \tag{2.18}$$

This expression clearly shows how, with these two devices, is not possible to

fully exploit the trigonometric nonlinearities $\cos\varphi$ and $\sin\varphi$ offered by the Josephson effect. In fact, as clear from expression (2.18), these two terms are respectively tuned with external flux by the bias coefficients $\cos\varphi_e$ and $\sin\varphi_e$, that are strictly linked by pitagorean relation $\sin^2\varphi_e + \cos^2\varphi_e = 1$.

In the rest of this manuscript, an approach to overcome this constraint will be introduced and experimentally demonstrated, constituting the original contribute of the author to the field.

2.2 Gradiometric SNAIL

As explained in the previous section, superconducting loops are key ingredients for implementing parametric processes but, with only one external flux bias, is not possible to completely explore the nonlinear effects provided by Josephson junctions. For this effort, it is possible to build a dipole made by a minimum of three branches that enclose at least two independently flux-biased superconducting loops.

A first demonstration of this approach has been performed by the author in [18, 38], where a symmetric rf-SQUID has been used as a building block of a traveling wave parametric amplifier. This work was inspired by the previously mentioned rf-SQUID based TWPA by Zorin [14, 15], and it was successfully proved that 3WM amplification can be provided with a doubly flux-biased superconducting dipole made by two loops. In this section, the gradiometric SNAIL will be introduced as an elementary block of a two-flux-biased superconducting circuit.

The Gradiometric SNAIL (G-SNAIL) is a SNAIL with two loops. Its concept is inspired by the symmetric rf-SQUID [18, 38] and the Asymmetric Threaded SQUID [39]. A G-SNAIL, represented in figure 2.7, is a simple two-loops superconducting dipole made by Josephson junctions, essentially built by "mirroring" a SNAIL with respect to the weakly nonlinear branch. The JJs on the side branches (colored in black in figure 2.7) are supposed equal, each one with a Josephson energy equal to αE_J, where E_J is the Josephson energy of a junction in the central branch (colored in purple in figure 2.7). This forms a two-loops device that can be flux-biased with two independent external magnetic fluxes. G-SNAIL potential energy is written as

$$\frac{U(\varphi)}{E_J} = -3\cos\frac{\varphi}{3} - \alpha\left[\cos\left(\varphi-\varphi_1\right) + \cos\left(\varphi-\varphi_2\right)\right] \tag{2.19}$$

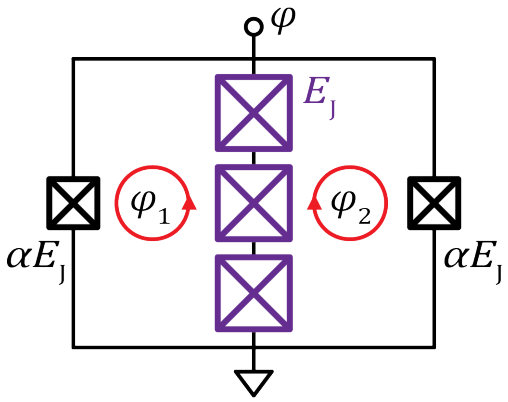

Figure 2.7: Gradiometric SNAIL. A symmetric dc-SQUID is shunted in the center with an array of three JJs, in order to form two superconducting loops. Each loop is then flux-threaded with two independent magnetic fluxes φ_1 and φ_2.

that, by introducing the sum and difference of bias phases

$$\begin{aligned} \varphi_+ &= \frac{\varphi_1 + \varphi_2}{2} \\ \varphi_- &= \frac{\varphi_1 - \varphi_2}{2} \end{aligned} \tag{2.20}$$

can be expressed in the compact form

$$\frac{U(\varphi)}{E_J} = -3\cos\frac{\varphi}{3} - 2\alpha\cos\varphi_-\cos\left(\varphi - \varphi_+\right). \tag{2.21}$$

This expression is equivalent to the SNAIL potential energy (2.16), when one introduces effective quantities

$$\begin{aligned} \alpha_{\text{eff}} &= 2\alpha|\cos\varphi_-| \\ \varphi_{\text{eff}} &= \begin{cases} \varphi_+ & \text{if } \cos\varphi_- > 0 \\ \varphi_+ + \pi & \text{if } \cos\varphi_- < 0 \end{cases} \end{aligned} \tag{2.22}$$

so reads as follows

$$\frac{U(\varphi)}{E_J} = -3\cos\frac{\varphi}{3} - \alpha_{\text{eff}}\cos\left(\varphi - \varphi_{\text{eff}}\right). \tag{2.23}$$

It is important to notice that expression for α_{eff} in (2.22) does not only include the geometrical α coefficient that has a direct correspondence with

the SNAIL α as in equation (2.16), but also an in-situ tunable coefficient $\cos\varphi_-$. For this reason, G-SNAIL flux tunability is extended with respect to a SNAIL, as α is now a parameter that can be externally modified. As a consequence, the whole term $\cos\varphi_- \cos(\varphi - \varphi_+)$ participates to the choice of expansion coefficients for the potential energy. In fact, it can be expressed as

$$\cos\varphi_- \cos(\varphi + \varphi_+) = c_e(\varphi_+, \varphi_-)\cos\varphi + c_0(\varphi_+, \varphi_-)\sin\varphi \tag{2.24}$$

where the bias parameters are defined as

$$\begin{aligned} c_{\mathrm{e}}(\varphi_+, \varphi_-) &= \cos\varphi_- \cos\varphi_+ \\ c_{\mathrm{o}}(\varphi_+, \varphi_-) &= \cos\varphi_- \sin\varphi_+. \end{aligned} \tag{2.25}$$

Introducing the plane (c_e, c_o), represented in figure 2.8, the expressions (2.25) describe a circle on such a plane when φ_+ and φ_- vary in the $[0, 2\pi)$ interval. From this representation is immediately clear the advantage of using a

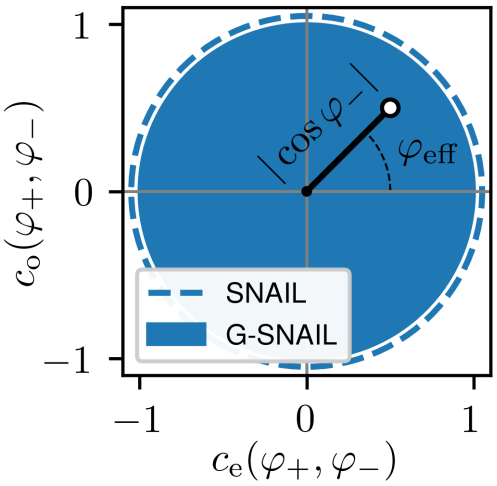

Figure 2.8: Bias coefficients plane. With a G-SNAIL is possible to operate over the whole solid circle, while a SNAIL only allows operating points belonging to the circumference.

doubly-flux-biased dipole: it can be operated on a 2D manifold instead of a single line. The G-SNAIL adds a radial degree of freedom to the standard SNAIL tunability on the bias coefficients plane in figure 2.8, with the capability of implementing a whole family of devices with a different design

parameter α within a single circuit. Note that a negative value of α_{eff} is equivalent to a π shift in the effective flux φ_{eff}. Nonlinear expansion c_3 and c_4 coefficients are, now, function of two bias parameters

$$\begin{aligned} c_3 &= -\frac{\sin\left[\dfrac{\varphi_0(\varphi_+,\varphi_-)}{3}\right]}{9} - 2\alpha\cos\varphi_-\sin\left[\varphi_0(\varphi_+,\varphi_-)-\varphi_+\right] \\ c_4 &= -\frac{\cos\left[\dfrac{\varphi_0(\varphi_+,\varphi_-)}{3}\right]}{27} - 2\alpha\cos\varphi_-\cos\left[\varphi_0(\varphi_+,\varphi_-)-\varphi_+\right] \end{aligned} \tag{2.26}$$

so a G-SNAIL has a much wider nonlinear tunability with respect to single-loop dipoles as rf-SQUIDs or standard SNAILs. In figure 2.9, a plot of expressions (2.26) clearly shows the enhanced tuning capabilities of the G-SNAIL, allowing to explore many combinations of nonlinear effects that were before constrained by the presence of a single flux-bias knob. An interesting

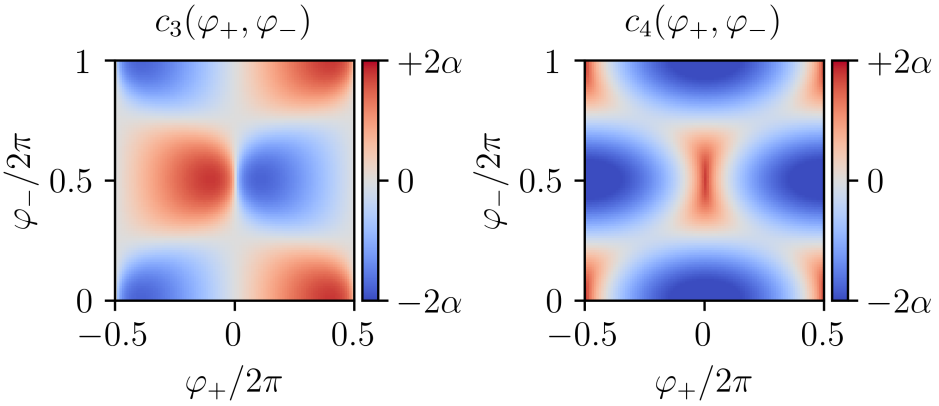

Figure 2.9: Nonlinear coefficients c_3 and c_4 for a G-SNAIL. With two flux-bias knobs is possible to tune 3WM (c_3) and 4WM (c_4) on a 2D space, allowing different combinations of nonlinear effects to be implemented on a single device.

feature of the G-SNAIL is the capability to keep one of the two coefficients to zero, for example, c_4, and still have a degree of freedom for tuning c_3. To show this, it is possible to define a curve γ_0 on the flux-bias plane (φ_+, φ_-), parametrized with a curvilinear parameter $s \in [0, 1]$, such that $c_4 = 0$ on each point of this curve, as in the left panel of figure 2.10. The right panel of

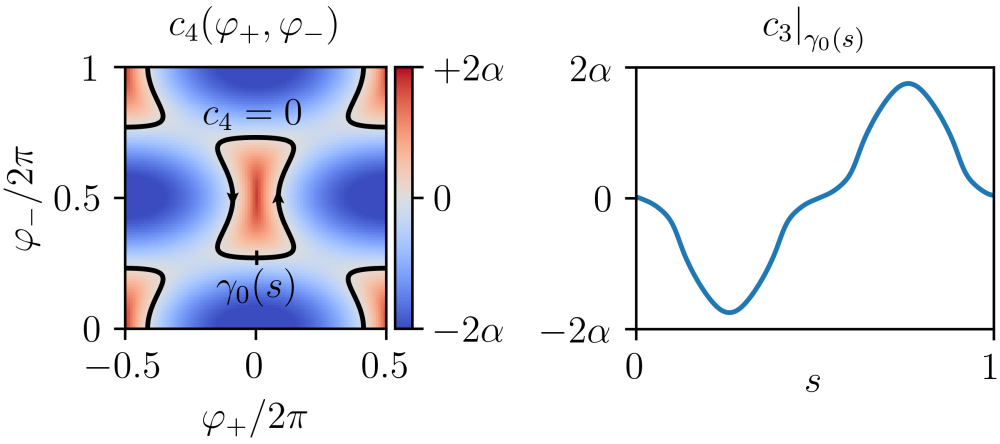

Figure 2.10: $c_4 = 0$ curves. 3WM coefficient c_3 can vary on a significant range when evaluated on the γ_0 curve such that $c_4 = 0$ on its points.

the same figure shows how c_3 can vary over a significant range $\sim (-2\alpha, 2\alpha)$ when evaluated along a $c_4 = 0$ curve.

In the following section, a superconducting resonator made by G-SNAILs will be discussed. It will be shown how its 2D flux-bias tunability can implement Kerr-free 3WM operations over a continuum of operating frequencies.

2.3 Gradiometric SNAIL Parametric Amplifier

A possible way to operate a superconducting inductive loop as a parametric amplifier is to embed it in a LC resonator, as in figure 2.2, in order to efficently implement 3WM operations around a resonance frequency ω. In this section, the Gradiometric SNAIL Parametric Amplifier (G-SPA) will be introduced, as an enhanced version of the SNAIL Parametric Amplifier (SPA) [21] that represents the state-of-the-art 3WM resonant parametric amplifier for the readout of superconducting qubits [22].

The fundamental block af a G-SPA is an array of M identical G-SNAILs (see figure 2.11) that are flux-biased with two independent magnetic fluxes. The fluxes can be delivered, for example, by two flux lines in which two currents are injected by independent generators. Considering the potential

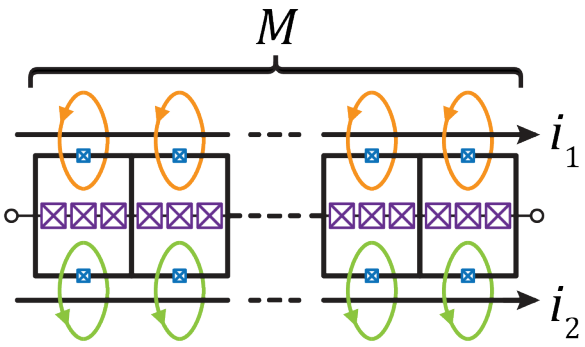

Figure 2.11: Array of G-SNAILs with two dedicated flux lines. Arraying allows to increase the maximum value of tunable inductance and, at the same time, dilute nonlinearity of the array. On the sides of the array, two flux-lines are driven by two independent current generators.

energy of a single G-SNAIL as in (2.21), for the array in figure 2.11 we have

$$\frac{U_a(\varphi)}{E_J} = -M\left[3\cos\frac{\varphi}{3M} + \alpha_{\text{eff}}\cos\left(\frac{\varphi}{M} - \varphi_{\text{eff}}\right)\right] \tag{2.27}$$

where φ is now the total phase drop across the array. Across each G-SNAIL, the phase drop will be φ/M in the hypotesis of identical cells. To understand the effect of arraying, let's compute the nonlinear expansion coefficients once a φ_0 equilibrium phase point is known. Following the same technique used for G-SNAIL, we have

$$\begin{aligned} c_3 &= -\frac{1}{M^2}\left\{\frac{\sin\left[\dfrac{\varphi_0(\varphi_+,\varphi_-)}{3M}\right]}{9} + 2\alpha\cos\varphi_-\sin\left[\frac{\varphi_0(\varphi_+,\varphi_-)}{M} - \varphi_+\right]\right\} \\ c_4 &= -\frac{1}{M^3}\left\{\frac{\cos\left[\dfrac{\varphi_0(\varphi_+,\varphi_-)}{3M}\right]}{27} + 2\alpha\cos\varphi_-\cos\left[\frac{\varphi_0(\varphi_+,\varphi_-)}{M} - \varphi_+\right]\right\} \end{aligned} \tag{2.28}$$

From there expressions for c_3 and c_4, it is clear how the presence of the array of M cells helps to suppress high order nonlinearities with a power law in M.

This is particularly useful if one aims at hitting a pure 3WM operation where the leading nonlinear term is c_3, thus it is desirable to suppress nonlinearities of order > 3. Arraying has also effect on the linear inductance of the array, defined as

$$L_a = \left(\frac{\Phi_0}{2\pi}\right)^2 \left(\frac{d^2U}{d\varphi^2}\right)^{-1} [\varphi_0(\varphi_+, \varphi_-)], \tag{2.29}$$

increasing its value by a factor of M

$$L_a = \frac{ML_J}{\dfrac{\cos\left[\dfrac{\varphi_0(\varphi_+,\varphi_-)}{3M}\right]}{3} + 2\alpha\cos\varphi_-\cos\left[\dfrac{\varphi_0(\varphi_+,\varphi_-)}{M} - \varphi_+\right]} \tag{2.30}$$

where $L_J = (\Phi_0/2\pi)^2 \frac{1}{E_J}$ is the equivalent inductance of a JJ in the central branch (colored in purple in figure 2.11) of each G-SNAIL forming the array. This come particularly handy if, for example, one would like to tune the resonance frequency of an LC resonator where the array is embedded. A proper choice of M can in fact increase the overall inductance without the need to directly increase the individual inductances of the junctions in the device: as linear Josephson inductance is inversely proportional to the critical current, is not possible to increase it without affecting the current dynamic range.

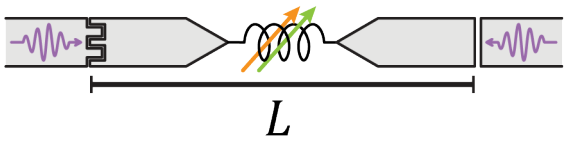

Figure 2.12: Gradiometric SPA. A doubly flux-biased dipole made with G-SNAILs, represented by an inductance crossed by two arrows, is placed in the middle of a $\lambda/2$ resonator that is capacitively coupled to two ports. On the left, a strongly coupled signal port is employed to feed the probe signal to the device while, on the right, a weakly coupled pump port is used to excite nonlinear processes as 3WM, for example, to generate amplification at signal port.

In order to implement a device that can be operated around a particular frequency ω with a certain bandwidth $\Delta\omega$, it is practical to embed our array of M G-SNAILs inside a microwave resonator with a certain bare resonance

frequency ω_0 and a coupling k to the input port (probed in reflection). To maximize the interaction between the electromagnetic field of the resonator and the nonlinear dipole, it is important to place it in correspondence of a current antinode of the resonator. Opting for a capacitively coupled $\lambda/2$ resonator, this will have maximum current in the middle, and that is where the dipole should seat. This thumb rule for the placement of a dipole inside a resonator is only valid if the dipole is much smaller than λ. In this G-SPA, while the resonator length L will be of the order of few millimiters, the dipole length will not exceed 200 μm. Consequently, it can be modeled as a lumped element and will have to be centered on a current antinode for optimal interaction with the electromagnetic field of the microwave resonator. A simplified schematic of the complete device is represented in figure 2.12 and is including a signal port (left, strongly coupled) and a pump port (right, weakly coupled) to easily deliver different microwave tones. Near the resonance frequency, the $\lambda/2$ resonator can be modeled by a lumped element LC series resonator, so a lumped circuit model can be made for the G-SPA. From the lumped model in figure 2.13, it is straightforward to compute the

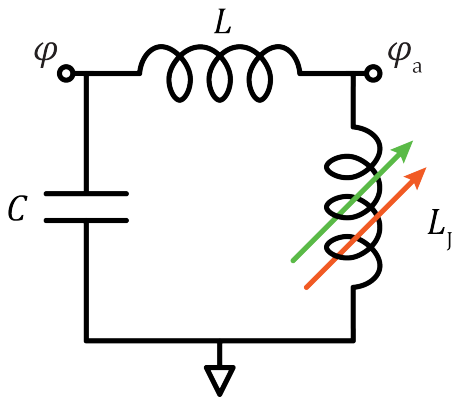

Figure 2.13: Lumped element model of a Gradiometric SPA. The $\lambda/2$ resonator is represented by a linear inductance L and a capacitance C. The array of G-SNAILs, represented by the inductance L_J tunable by two external parameters (two arrows), is electrically in series with the linear inductance of the resonator.

Hamiltonian of the G-SPA, once the active-node phase φ has been identified as in figure 2.13. Following the procedures described in the first chapter, the Hamiltonian of the device reads as

$$H = \hbar\omega(\varphi_+, \varphi_-)\mathbf{a}^\dagger\mathbf{a} + g_3(\varphi_+, \varphi_-)(\mathbf{a} + \mathbf{a}^\dagger)^3 + g_4(\varphi_+, \varphi_-)(\mathbf{a} + \mathbf{a}^\dagger)^4 \quad (2.31)$$

where ω, g_3 and g_4 are variable with the bias fluxes (φ_+, φ_-). The potential energy of the lumped G-SPA can be written as

$$U(\varphi) = \frac{1}{2} E_L [\varphi - \varphi_a(\varphi)]^2 + U_a [\varphi_a(\varphi)] \tag{2.32}$$

where the relation $\varphi_a(\varphi)$ is implicitly defined from the current conservation equation

$$E_L(\varphi - \varphi_a) - \frac{dU_a}{d\varphi_a} = 0. \tag{2.33}$$

This equation is derived from the consideration that the resonator linear inductance L and the G-SNAILs array tunable indutance L_J are in series, as in figure 2.13, thus the current flowing in each of them has to be the same. In order to obtain a representation of these three coefficients in terms of expansion coefficients of the G-SNAILs array, the procedure in [21] is described. It is useful to introduce the participation ratio p of the array of G-SNAILs, defined as

$$p \triangleq \frac{d\varphi_a}{d\varphi} = \frac{E_L}{E_L + \dfrac{d^2 U_a}{d\varphi_a^2}} = \frac{L_a}{L + L_a} \tag{2.34}$$

This quantity acts as a phase divider coefficient that describes how the phase drop φ_a is linked to the resonator phase φ, when the circuit is supposed to be linear. The expansion coefficients $\tilde{c}_n = \frac{1}{n!} \frac{d^n U}{d\varphi^n} \big|_{\varphi_0}$ of the function (2.32) can now be computed. First order coefficient $\tilde{c}_1$ can be expressed as

$$\begin{aligned} \tilde{c}_1 &= E_L[\varphi_0 - \varphi_a(\varphi_0)] \left[1 - p(\varphi_0)\right] - \frac{dU_a}{d\varphi_a}[\varphi_a(\varphi_0)] p(\varphi_0) \\ &= E_L[\varphi_0 - \varphi_a(\varphi_0)] \end{aligned} \tag{2.35}$$

where last identity is granted by current conservation equation (2.33). Being φ_0 defined such that $\tilde{c_1}(\varphi_0) = 0$, evaluating current conservation (2.33) for $\varphi = \varphi_0$ results in

$$\frac{dU_a}{d\varphi_a} [\varphi_a(\varphi_0)] = 0, \tag{2.36}$$

as the first term of the equation is exactly $\tilde{c}_1$. Equation (2.36) shows how a φ_0 that minimizes the total potential energy (2.32) corresponds to a φ_a value that minimizes the array potential energy (2.27). As a consequence, it

can be stated presence of the linear inductance in the circuit in figure 2.13 does not affect the position of the potential energy minimum. This result is valid, in general, for any nonlinear dipole in series with a linear inductor, regardless from the particular potential energy function implemented by the array, that has not been explicitly expressed. Higher order coefficients can then be expressed as follows

$$\begin{aligned}\tilde{c}_2 =& \frac{E_L}{2!}\left[1 - p(\varphi_0)\right] \\ \tilde{c}_3 =& -\frac{E_L}{3!}\left[\frac{dp}{d\varphi}(\varphi_0)\right] \\ \tilde{c}_4 =& -\frac{E_L}{4!}\left[\frac{d^2p}{d\varphi^2}(\varphi_0)\right]\end{aligned} \tag{2.37}$$

The derivatives of p are expressed as

$$\begin{aligned}\frac{dp}{d\varphi} =& -\frac{1}{E_L}p^3 c_3 \\ \frac{d^2p}{d\varphi^2} =& -\frac{1}{E_L}p^4\left[c_4 - \frac{3c_3^2}{c_2}(1-p)\right]\end{aligned} \tag{2.38}$$

and, finally,

$$\begin{aligned}\tilde{c}_2 &= \frac{1}{2!}pc_2 \\ \tilde{c}_3 &= \frac{1}{3!}p^3 c_3 \\ \tilde{c}_4 &= \frac{1}{4!}p^4\left[c_4 - \frac{3c_3^2}{c_2}(1-p)\right]\end{aligned} \tag{2.39}$$

The Hamiltonian of the circuit can then be expressed as

$$H = E_C\boldsymbol{N}^2 + \tilde{c}_2\boldsymbol{\varphi}^2 + +\tilde{c}_3\boldsymbol{\varphi}^3 + \tilde{c}_4\boldsymbol{\varphi}^4 \tag{2.40}$$

where $\boldsymbol{N}$ is the number operator that describes the charge stored in the capacitor C and $\boldsymbol{\varphi}$ is the phase operator related to the equivalent flux in the total inductance $L + L_a$. By introducing creation and annihilation operators, respectively $\boldsymbol{a}^\dagger$ and $\boldsymbol{a}$, the expression (2.31) can be retrieved, where the coefficients of the Hamiltonian are now expressed in terms of expansion

coefficients of the array potential energy U_a as

$$\begin{aligned} \omega =& \frac{1}{\sqrt{C\left(L + c_2^{-1}\right)}} \\ g_3 =& \frac{p^2}{6}\frac{c_3}{c_2}\sqrt{\frac{\omega E_C}{\hbar}} \\ g_4 =& \frac{p^3}{12}\left[c_4 - \frac{3c_3^2}{c_2}\left(1-p\right)\right]\frac{E_C}{c_2}. \end{aligned} \tag{2.41}$$

From these quantities, it is now possible to obtain an expression for the detrimental Kerr effect that affects 3WM behavior of superconducting circuits, we would like to suppress.

2.3.1 Kerr-free lines in a G-SPA

Kerr is a nonlinear effect that is present, in general, in any nonlinear superconducting circuit. It arises from the dispersion of transition energies as a function of the level index n and is defined as

$$K \triangleq \frac{d^2E(n)}{dn^2} \tag{2.42}$$

such that the energy of an oscillator can be corrected with a quadratic perturbative term

$$E(n) \approx \left(\frac{1}{2} + n\right)\hbar\omega + \frac{K}{2}n^2. \tag{2.43}$$

As will be shown later, this Kerr coefficient K results in a resonance frequency shift for the G-SPA, depending on the number of photons n that populate the resonator. Considering the Hamiltonian (2.31), it is useful to compute $E(n) = \langle n| H |n\rangle$ to have a first estimate of the transition frequencies as a function of n. In fact, while the linear term $\boldsymbol{a}^\dagger\boldsymbol{a}$ and the fourth order one $(\boldsymbol{a}+\boldsymbol{a}^\dagger)^4$ contribute to $E(n)$ at first order, the third order one $(\boldsymbol{a}+\boldsymbol{a}^\dagger)^3$ will only contribute as a second order perturbation as $\langle n|\left(\boldsymbol{a}+\boldsymbol{a}^\dagger\right)^3|n\rangle = 0\ \forall n$. Then, g_3 can be treated as a perturbation to the Hamiltonian H. By only considering the linear and fourth order terms of the G-SPA Hamiltonian, a

first estimation of the transition energies $E_0(n)$ reads

$$\begin{aligned} E_0(n) = \langle n| H |n\rangle = \langle n| \hbar\omega \boldsymbol{a}^\dagger \boldsymbol{a} + \\ g_4(\boldsymbol{a}^{\dagger 2}\boldsymbol{a}^2 + \boldsymbol{a}^2\boldsymbol{a}^{\dagger 2} + \\ \boldsymbol{a}^\dagger \boldsymbol{a}^2 \boldsymbol{a}^\dagger + \boldsymbol{a}\boldsymbol{a}^{\dagger 2}\boldsymbol{a} + \\ \boldsymbol{a}^\dagger \boldsymbol{a}\boldsymbol{a}^\dagger \boldsymbol{a} + \boldsymbol{a}\boldsymbol{a}^\dagger \boldsymbol{a}\boldsymbol{a}^\dagger + \dots) |n\rangle \end{aligned} \tag{2.44}$$

where the non-conservative contributions in the expansion of the quartic $(\boldsymbol{a} + \boldsymbol{a}^\dagger)^4$ term have been neglected. In fact, these are not relevant in a first order estimation as their expected value on a state $|n\rangle$ will be zero. On the contrary, each of the six terms in the expansion (2.44) will contribute to the Kerr-term with a factor proportional to n^2. In total, the fourth order term will deliver a quantity $12g_4$. From second order perturbation theory, is also possible to express the contribution of the g_3 term at lowest order as $-5\frac{g_3^2}{\omega}$ so, the total Kerr will be

$$K = 12g_4 - 5\frac{g_3^2}{\omega} \tag{2.45}$$

that, in conjunction with the equations (2.41), can be finally expressed as a function of external fluxes $K(\varphi_+, \varphi_-)$. From this expression it is now possible to define Kerr-free lines (KFLs). A KFL is a curve γ_{KFL} on the (φ_+, φ_-) bias fluxes plane such that $K = 0$ for each point of such a curve. In chapter 3, simulations of Kerr-free lines will be discussed, and their experimental characterization is presented in chapter 4.

2.3.2 Three-wave mixing amplification

A G-SPA can be three-wave mixing enabled if flux-biased in a point where third order nonlinearity g_3 of the Hamiltonian (2.31) is non-zero. In fact, by applying an additional, strong microwave pump tone, it is possible to excite a three-wave mixing process that can deliver gain at the resonant frequency $\omega/2\pi$, within a certain bandwidth k [40]. Pumping at exactly twice the resonance frequency of the G-SPA, it is possible to implement a degenerate three-wave mixing, where two signal photons interact with a pump photon in order to increase their number. To highlight this effect, it is useful to consider the annihilation operator of the G-SPA Hamiltonian to be transformed as $\boldsymbol{a} \to \boldsymbol{a} + \boldsymbol{I}\alpha e^{i\omega_p t}$, where the first term $\boldsymbol{a}$ corresponds to the signal mode, while, the term $\boldsymbol{I}\alpha_p e^{i\omega_p t}$, represents a coherent pump at frequency $\omega_p/ \approx 2\omega$

and amplitude α_p, strong enough to be considered classical in the analysis. Thus, Hamiltonian reads

$$H = \hbar\omega \boldsymbol{a}^\dagger \boldsymbol{a} + g_{aa}(\boldsymbol{a}^2 e^{i\omega_p t} - h.c.) + \dots \tag{2.46}$$

where terms not responsible for gain are absorbed in the dots. Gain is enabled by the coefficient $g_{aa} = g_3\alpha_p$, so can be obtained only if $g_3 \neq 0$ and provides a strong signature of three-wave mixing operations. The additional terms in the Hamiltonian (2.46), despite not being directly involved into the amplification, can harm its performance as they can lower the efficiency of three-wave mixing process or detune the resonance frequency ω from the desired value. Among these terms, the Kerr is the most important to suppress, as it arises from a combination of the most relevant expansion coefficients of the potential energy of a G-SPA, namely $\tilde{c}_2$, $\tilde{c}_3$ and $\tilde{c}_4$. The advanced Hamiltonian tuning capabilities of a G-SPA can be employed to suppress as much as possible these detrimental terms, keeping the Hamiltonian (2.46) in its simplest form for different values of the resonance frequency. This is only possible with the additional phase-bias degree of freedom φ_-, provided by the Gradiometric SNAIL. An experimental demonstration of Kerr-free three-wave mixing amplification at different operating frequencies is presented in chapter 4.

Chapter 3

Design and fabrication of a GSPA

3.1 Numerical simulations

To design an operative G-SPA, it is necessary to consider some constraints that depend on the particular application, the employed materials, but also on the limitations of the measurement capabilities of the hardware for its experimental characterization. First, let's consider frequency specs. As the chain of microwave components (detailed in the last chapter) has a finite frequency bandwidth, the target maximum frequency $f\max$ of the G-SPA (at zero external bias, with no trapped flux), should be lower than the maximum frequency of the setup. Quantitatively, it is desirable to acquire the frequency response up to at least $f_{\max}+k$, where k is the total bandwidth of the G-SPA, in order to easily measure the whole resonance curve centered at $f_{\max}$. For the device presented in this manuscript, a maximum operating frequency of about 9.2 GHz has been chosen. In order to hit this target frequency with the experimental device, it is important to balance the inductive contributes to the resonance of both the nonlinear array of G-SNAILs and the linear resonator. In fact, the resonance frequency can be tuned by both changing the length of the $\lambda/2$ resonator and changing parameters of the array as M, α and E_{J}. Is important to keep in mind that changing either of the two contributions to the resonance will also modify the array participation ratio p, defined in the expression (2.34). To fully explore the tuning capabilities of the G-SNAILs, the maximum allowed value $\alpha = 0.15$ has been chosen. In

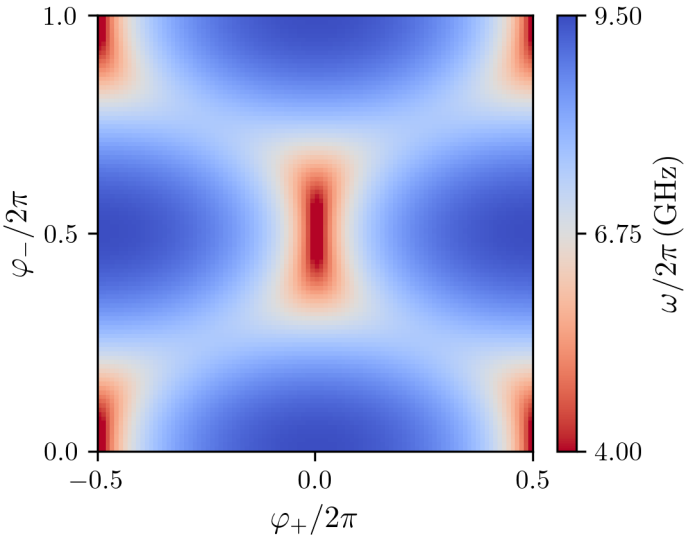

Figure 3.1: Numerical simulations of the resonance frequency of a G-SPA as a function of the bias phases φ_+ and φ_-. The response is periodical in both phases, and the transformation $\varphi_\pm \to \varphi_\pm + \pi$ keeps the response unchanged, as predicted from the model.

fact, for $\alpha > 0.15$, a G-SNAIL can implement a multi-well potential energy function that can harm its tunability by trapping the phase particle in the wrong minima and requiring to reset it to the initial state before proceeding. At this point, as

$$f_{\max} = \frac{f_0}{\sqrt{1 + \dfrac{L_J M}{L_0\left(\frac{1}{9} + 2\alpha\right)}}} \tag{3.1}$$

where $L_0 = Z_0/\omega_0$ is the inductance of the bare $\lambda/2$ resonator and $Z_0 = 50$ Ω its intrinsic impedance, it is possible to retrieve a value for the quantity $L_J M$ that fixes the array characteristics. As in a standard SPA $M = 20$ has been chosen [21, 22], thus the solution L_J is known once the bare resonance frequency of the resonator f_0 is fixed. Once a target L_J is known, one can design the junctions in order to have the right area given the critical current density of the process. The experimental data presented in this thesis was measured from a G-SPA with a maximum frequency of about 9.25 GHz, corresponding to a value $L_J \approx 20$ pH. It is then possible to numerically

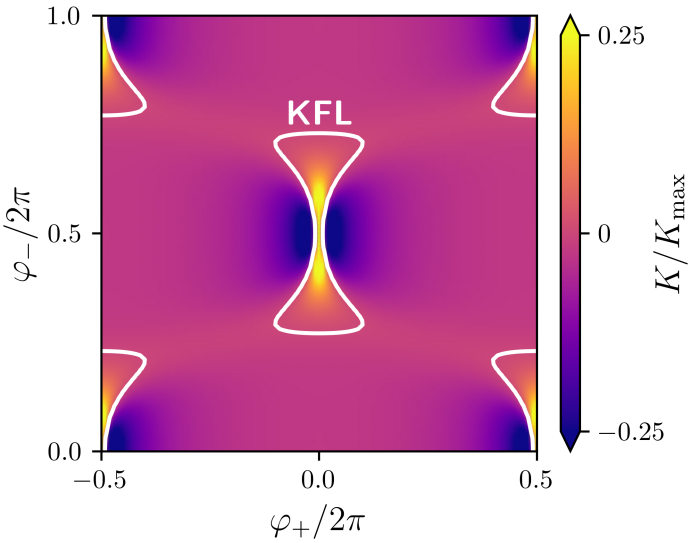

Figure 3.2: Numerical simulations of the Kerr coefficient as a function of bias phases φ_+ and φ_-. Kerr shares same periodic structure as frequency response. Kerr-free lines are traces over the Kerr plot, identifying the possible combinations of bias fluxes that suppress the Kerr.

simulate the resonance frequency as a function of the two bias phases φ_+ and φ_-, by computing the shape of the potential energy function and then expanding it around its minima. A 2-D plot of the resonance frequency can then be produced (figure 3.1), showing what should be expected from experimental mesurements, in order to validate the G-SPA model. This resonance frequency simulation has been performed with the following parameters set: $\alpha = 0.145$, $\omega_0/2\pi = 15.61$ GHz, $L_\text{J} = 27$ pH and $Z_0 = 50\ \Omega$. These values were extracted by least-square fitting the experimental data shown in chapter 4 with the model (2.41) for ω, described in chapter 2. With an expansion of the potential energy up to the fourth order, it is also possible to estimate the Kerr effect with the expression (2.45) as a function of the two bias phases, represented in figure 3.2. Regions of particular interest are those where the Kerr is suppressed, in order to implement pure and clean 3WM operations. While with a single flux-knob it is only possible to identify a Kerr-free point, here, with two flux bias knobs, Kerr can be suppressed on a 1D variety, namely a KFL. The additional flux bias degree of freedom can be employed, for example, to change the resonance frequency of a G-SPA while preserving

Kerr-free operation.

3.2 CAD Simulations

CAD simulations were performed in order to characterize and validate the design. ANSYS HFSS software was employed to analyze the linear response of the device (see figure 3.3), where the JJs have been replaced by linear inductances with values L_J and L_J/α, for big and small junctions respectively. In this way, it was possible to converge on an overall resonator length $L \approx 2.8$ mm, including the array of G-SNAILs, that ensured the correct frequency placement of the device. This analysis also took into account the particular geometry and the coupling to external environment because of signal, pump and flux-bias ports. Signal port interdigital coupling capacitor, as well as the pump port gap capacitor shapes, were optimized in ANSYS in order to implement couplings of desired strength. Losses due to the flux lines were underestimated by HFSS, as from simulations we would have expected < -20 dB losses. In the real device, losses that can go beyond this value have been measured. This is probably due to the surrounding electromagnetic environment that was not taken into account in the simulations. In fact, the experimental sample sits in a PCB with 6 ports: 2 RF ports for signal and pump, and 4 DC ports for the current bias of the flux lines. These latter ones are arranged two per side, in order to provide, for each flux line, a feed port and a return port for the bias current. The two ports are also shunted on the PCB with 5 Ω SMD thin-film metallic resistors (see figure 3.12), in order to provide a low resistive path in case one of the superconducting flux lines switches to normal if its critical current is exceeded. This is particularly important when implementing thin aluminum lines, as these are pretty fragile and could easily blow-up with too much ohmic power dissipation. The flux lines were implemented with a width of 5um and a distance from the device of 5um, in order to provide enough flux before their critical current was reached. This resulted in a high coupling between the device and flux lines, providing non-negligible internal losses. To estimate a reasonable geometry for the flux lines that would guarantee reaching a flux quantum for both φ_+ and φ_- bias phases and, at the same time, not require a too high current, magnetostatic simulations with ANSYS Maxwell software were performed. By taking advantage of the symmetry of the device and the linearity of the magnetic problem (neglecting Meissner effect, not significant

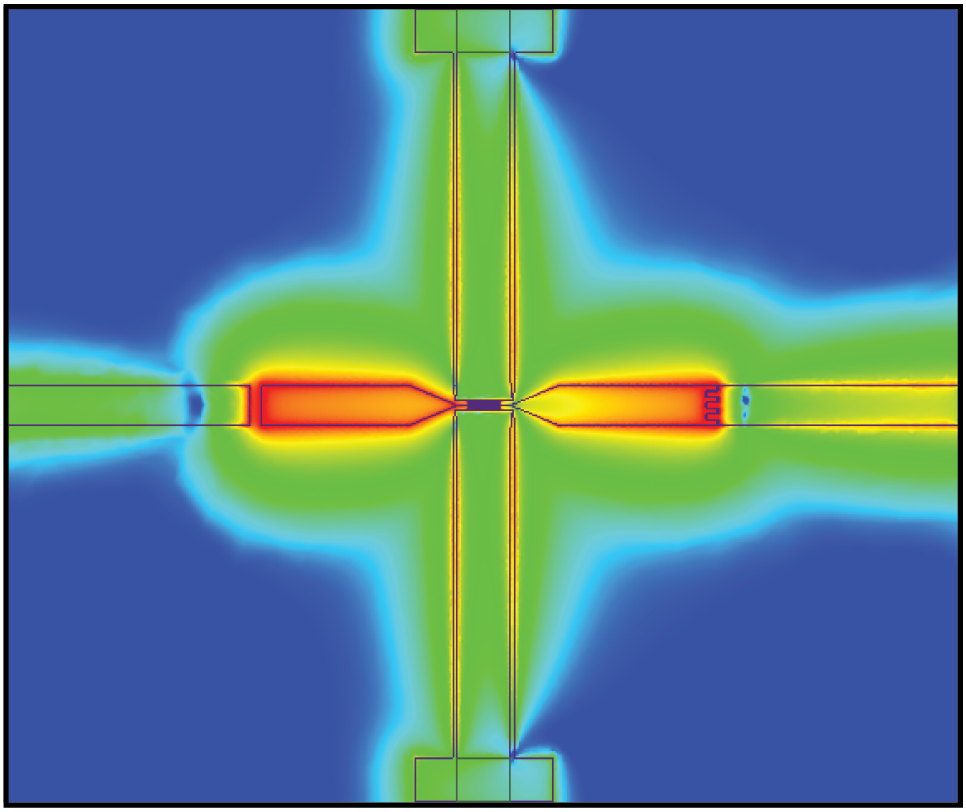

Figure 3.3: HFSS simulation for the device with shorted JJs. The absolute value of the electric field (blue is low intensity, red is high) is plotted on the substrate surface for the $\lambda/2$ resonance mode. It can be seen that the coupling to the flux lines is not negligible, as the electric field propagates along these. This suggests that charge coupling should be taken into account when designing on-chip flux lines.

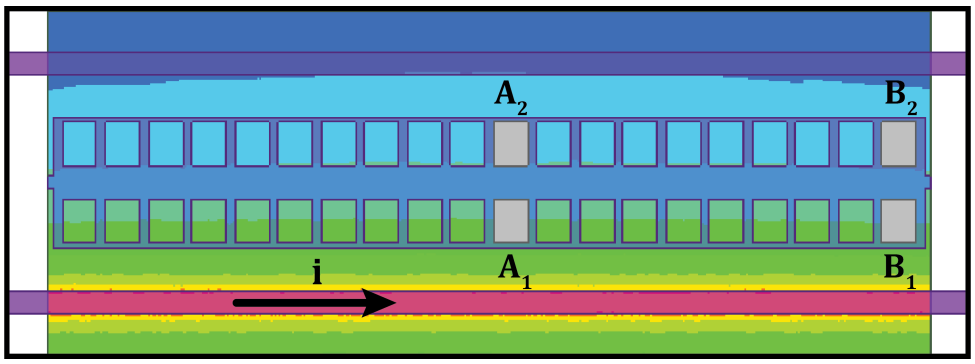

Figure 3.4: Magnetostatic simulation for the extraction of flux-bias couplings of the G-SPA. To estimate the flux gradient along the 20 cells array, as well as direct and cross couplings, the flux at four loops A_1, A_2, B_1 and B_2 is estimated when the magnetic field is excited by a one flux line only.

for our purposes), simulations were performed with only one current-biased flux line, while keeping the other unbiased with no flowing current. These simulations provided important feedback regarding the homogeneity of the flux along the direction of the array of G-SNAILs, a crucial feature to guarantee that all 20 cells are flux-threaded with the same fluxes for each loop, thus implementing the correct potential energy function for each value of φ_+ and φ_-. An acceptable homogeneity was achieved by having the flux-lines protruding on both sides of the array, in order to appear almost as infinite, parallel lines from the flux-bias point of view. With ANSYS Maxwell software it was also possible to estimate the flux supplied to a loop on the side of the biased line, and compare it to the flux supplied to a loop on the opposite side. This was important in order to understand how much tunability was possible to achieve in terms of φ_+ and φ_-, when biasing with side currents i_1 and i_2. The "cross-flux-bias" enhances the tunability of φ_-, while suppresses the φ_+ one. This wouldn't be a problem if flux lines were supporting high currents but, being entirely made by aluminum, and with a section of about $0.1\mu\text{m} \times 5\mu\text{m}$, they are limited to few mA of flowing current, if perfectly fabricated. The simulations allowed to extract mutual inductances between the biased flux line and four loops, chosen as in figure 3.4. With reference to the image, the four mutual inductances were estimated as

M_{A_1}	M_{A_2}	M_{B_1}	M_{B_2}
0.81 pH	0.38 pH	0.78 pH	0.36 pH

so the non-homogeneity of the flux along the array is acceptably $\approx 3\%$, while the difference between direct and cross flux is $> 50\%$, providing sufficient separation between the magnetic fields generated by each bias line.

3.3 Fabrication

The fabricated samples are based on aluminum as superconducting metal and aluminum oxide as insulator for the barrier of the tunnel Josephson junctions, everything deposited on an intrinisic silicon substrate. In order to implement a ground plane for the microstrip resonator, the employed wafers were previously covered on the back with a silver metal layer. To fabricate Josephson tunnel junctions the Dolan bridge technique has been employed, facilitating the deposition of both JJs and metallic layers (resonator, flux lines, capacitors etc.) with a single fabrication step.

The Dolan bridge technique [41, 42] is based on the fabrication of a resist mask where "suspended resist bridges" are employed to shadow certain regions of the substrate from the evaporation of the employed metal. This allows to create controlled overlaps between different metal layers when it is possible to choose their evaporation angles. In this section, the fabrication techniques employed for the realization of a G-SPA are described.

After a intrinsic silicon wafer has been back-covered by a metallic layer, the fabrication of the resist mask takes place. As already mentioned, the whole fabrication relies of the Dolan bridge technique. In order to be able to create suspended structures, it is necessary to employ two resists that have different sensitivity to the e-beam writing operation (cite papers). In fact, a bridge is formed by "digging" around and under a certain region of resist, leaving just a stripe hanging from two sides. With reference to figure 3.5: A first, "soft" resist of type MMA(8.5)MAA EL13 is spinned at 3000 rpm for 90 s on the substrate to reach a thickness $t_\mathrm{s} \approx 800$ nm, then baked for 1 minute at 175°C. Then a second, thinner layer of "harder" resist of type 950k PMMA A4 is spinned at 2000 rpm on top of the first one to reach a thickness $t_\mathrm{h} \approx 150$ nm, and baked as well for 15 minutes at 175°C. This completes the spinning of the resist layers, and the wafer is ready to be "activated" by an electron-beam lithography process.

The electron-beam lithography employs a very narrow, low current ($\sim$ 1/50 nA) and high-voltage ($\sim$ 100 kV) electron beam that can be positioned on a wafer with high precision, thanks to variable deflectors that orient the

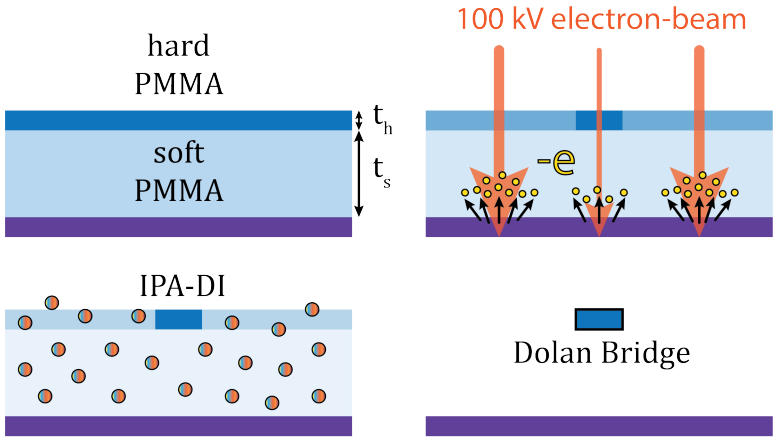

Figure 3.5: **a**. Cartoon of a wafer section for the fabrication of the Dolan bridge. A soft, thick PMMA layer is spinned of the substrate, then covered by an harder and thinner one. **b**. An electron-beam lithography is performed on the spinned wafer. A 100 kV beam is delivered on the regions where both the PMMAs have to be removed, with a high dose where both resists need to be removed and lower dose where the suspended bridge should be positioned. After the beam impacts the substrate, the latter backscatters electrons that activate the surrounding resist, spreading in a circle with a radius of ≈ 6 μm. This activates only certain regions for the development process, depending on the doses employed. **c**. An IPA-DI developer is employed to dissolve the regions activated by the e-beam lithography. **d**. The non-activated hard resist is suspended on top of the substrate, forming a Dolan bridge.

beam in two directions. The purpose of this step is to deliver electrons to the region of resist that need to be dissolved (in this case, a positive resist), in order to fabricate the resist mask that will effectively shape the sample in the deposition step. Because electrons are collected by the substrate, they travel all the way through the two resists before reaching the cathode. This implies that, over time, the bottom resist layer can be activated before the top one, by delivering a dose of electrons that is sufficient to activate the former only. With this technique, it is possible to activate all the resist except for a thin strip of hard PMMA, that will not undergo dissolution during the development process thus forming a Dolan bridge. In order to deliver the right dose of electrons in the right areas of the spinned wafer, it is possible to control the beam current i_{B} and the speed with which the beam will sweep on a certain region. In fact, the choice of beam current and sweep speed selects the charge-per-area-unit that the e-beam will deliver to the wafer. Usually, big features ($\simeq 0.1 - 1$ mm) are written by using high currents ($\simeq$ 20/40 nA) while smaller, more sensitive features are written with lower currents ($\simeq$ 2/5nA). In this way, the writing time can be kept reasonable ($\simeq$ 10 mins) also for big areas to be written. After the resist is activated by e-beam writing, the mask development is performed by diving the activated sample in a solution of IPA-DI 70/30, kept at 6C° and for a total time of 120s. The time, as well as the temperature, are crucial factors in order to deliver optimal results and, in general, the doses to use for the writing of a Dolan bridge strongly depend on these parameters.

Figure 3.6 shows a SEM picture of suspended and collapsed Dolan bridges after the development. In order to be able to see the resist bridges, the developed sample has been metallized with gold sputtering. The picture clearly shows how the resist, after e-beam and developement, form suspendend structures, i.e. Dolan bridges. These bridges are hanging from both sides thanks to resist patches that were not written at all, thus not being dissolved during development and providing sustain to the more delicate parts of the mask. If an excessive dose is delivered in the proximity of a bridge, or the development is performed for too long or at too high temperature, it is possible for a bridge to collapse, detaching itself from either or both sides thus falling onto the substrate. This makes the mask non operable for the deposition of Josephson junctions, that could still form, but with very weird and uncontrolled shapes. A bridge collapse usually results in a short-circuit shunting the junction. It is also possible to have "underdeveloped" bridges (see fig 3.10), where the dose delivered to the resist under the bridge was not high enough in order

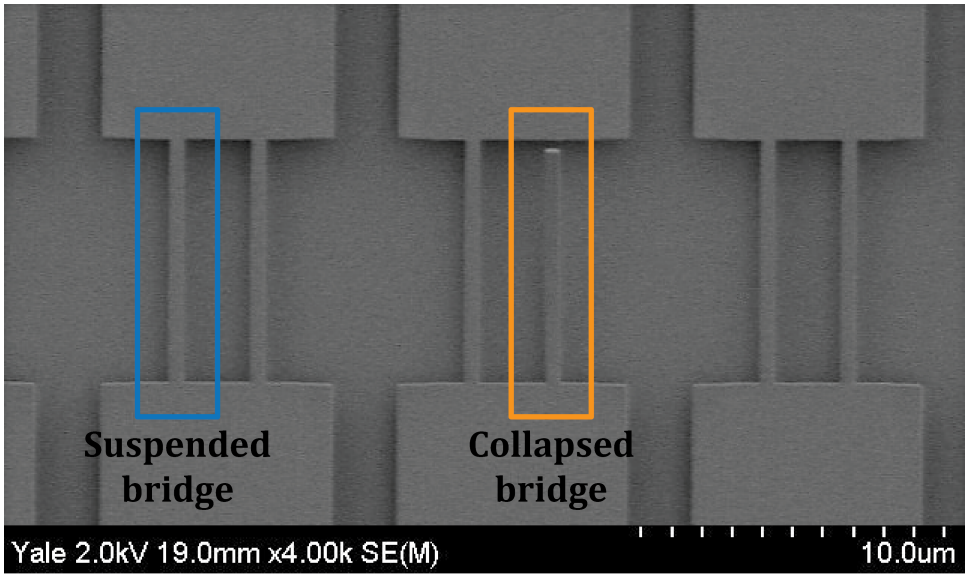

Figure 3.6: SEM image of gold-covered (with sputtering) Dolan bridges after development. Suspended bridges are hanging from both sides to two non-developed PMMA patches. If an excessive charge dose is delivered in the neighborhood of a bridge, it can collapse and won't be employable for the deposition of a Josephson junction.

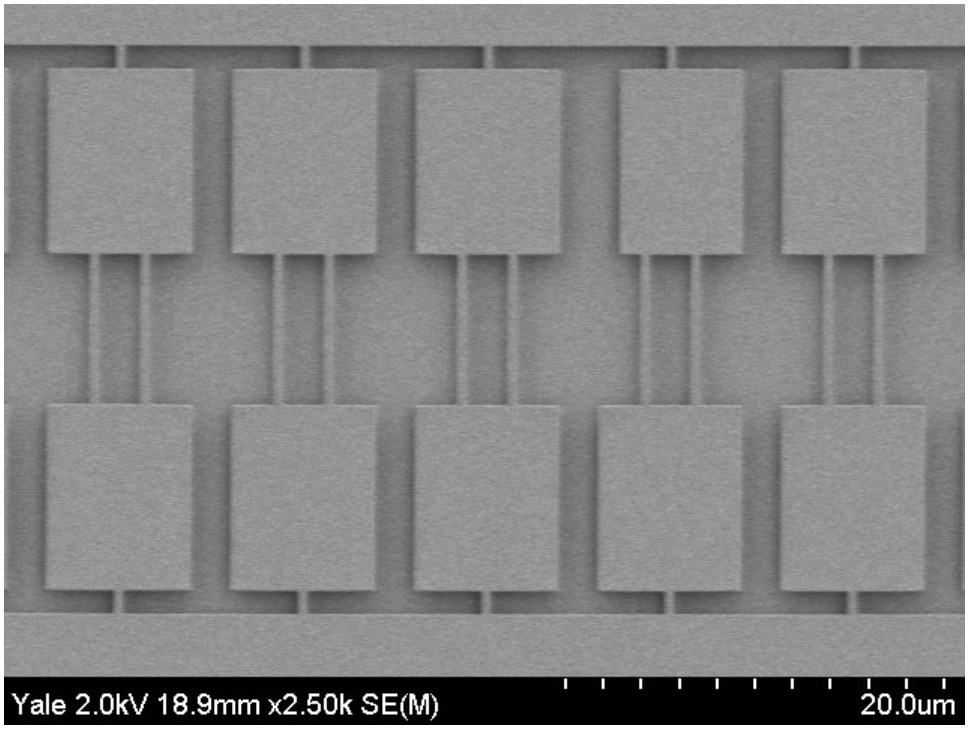

Figure 3.7: SEM image of gold-covered (with sputtering) resist mask for an array of G-SNAILs. Dolan bridges are fabricated for the deposition of both small and big junctions.

to dissolve it completely. This unwanted effect is more subtle of the bridges fall, being not visible before the fabrication process is complete. In general, every time a new mask is designed, this requires a calibration of the e-beam doses to assign to each feature. A complete mask for the G-SPA is shown in figure 3.7, where all the bridges are correctly formed for both small junctions (on the two sides of each G-SNAIL) and big junctions (arrayed on the center of each G-SNAIL).

After the mask is correctly fabricated, the sample undergoes the deposition of metal and oxidation layers for imprinting the design. The technique employed to deposit Josephson junctions with Dolan bridges is shown in figure 3.8. After an ArO_2 beam, with a ratio 3:1, is employed to clean the mask and substrate exposed surface from possible residues, a first layer of aluminum is deposited with an angle of $+45°$, in a controlled vacuum chamber at a base pressure $\sim 10^{-9}$ Torr. The function of the bridge is to provide

a shadowing of the substrate on a certain region, in order to not have any metal deposited on it [41] . Then, after this first step, the sample is transferred in an oxidation chamber that gets filled of ArO_2 molecules, with a ratio 85%/15%. The oxidation is performed for 7 minutes with a pressure ≈ 10 Torr , in order to grow aluminum oxide AlOx on top of the first layer. This forms a thin tunnel barrier that determines the critical current density of the fabrication process. A third step is performed, where aluminum is again deposited, but with an opposite angle $-45°$ with respect to the first metal layer. This time, the bridge will shadow in the opposite direction, allowing the formation of a tunnel junction in the region below it. Finally (not shown in the figure), an additional oxidation is performed in order to controllably grow aluminum oxide on the top of the whole sample shielding the sample from the room environment. In fact, as the air humidity level changes with the seasons, without this shielding oxide the same recipes could result in different critical current densities for fabrications performed in different times of the year. After the sample is retrieved from the evaporator system, it is necessary to remove all the unwanted aluminum that is sticking to the mask. This step, namely the "liftoff", is performed by soaking the wafer in pure N-Methyl-2-pyrrolidone (NMP) at a controlled temperature of 75 °C, at least for 90 minutes. Then, the sample is cut with a dicing machine, in order to retrieve the correct size of the chips before mounting. If the process has been successful, it is possible to see the junctions with a SEM. Figure 3.9 shows the array of three JJs in the center of a G-SNAIL, correctly formed after a successful deposition. These JJs were obtained with two bridges, each one with nominal width of 0.5 μm, a length of 8 μm and with an edge-to-edge distance of 2.2 μm. This resulted in three JJs, where the two on the sides of the array have an effective area of $8\mu\text{m} \times 0.67\mu\text{m}$, while the one in the center has a slightly larger effective area of $8\mu\text{m} \times 0.75\mu\text{m}$. If the fabrication process hasn't been successful because of underdeveloped bridges, the junctions would appear as in figure 3.10, with a rounded shape and cut off corners. This happens because, instead of digging a sharp, rectangular hole below the bridge, the development doesn't homogeneously remove the soft resist, that will keep sticking under the sides of the bridge, giving it the shape of an arc. In this way, the shadow that the underdeveloped bridge will project on the substrate will result in a rounded shape of the junctions. Notice how this degree of underdevelopment only affects the first and last junctions in the center of each G-SNAIL. In fact, while these two are obtained by the metal going below the bridge, the center junction has a shape that depends on the

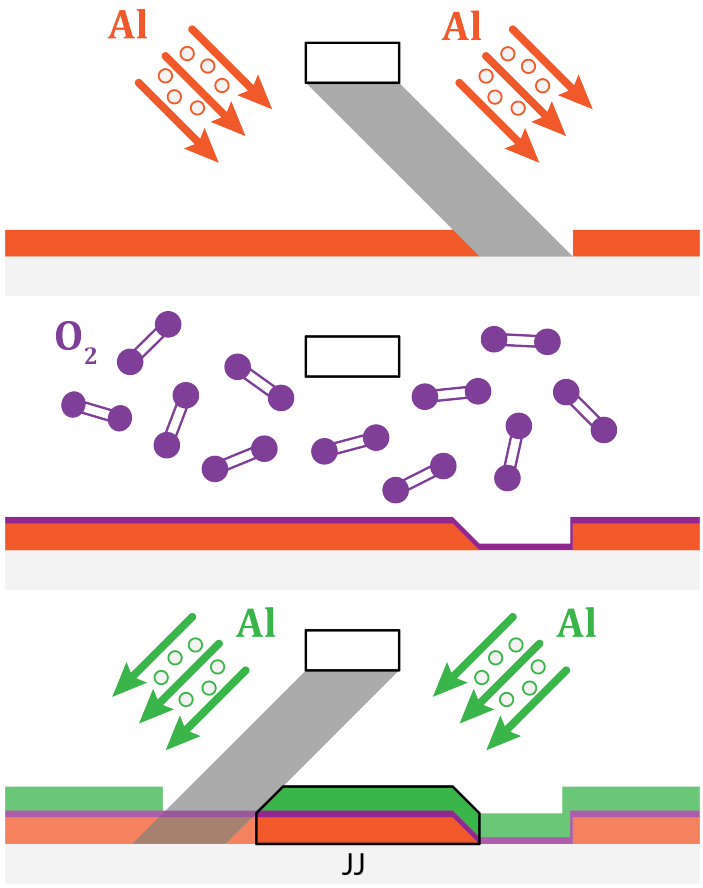

Figure 3.8: Dolan bridge process for the deposition of a tunnel Josephson junction. A Dolan bridge is employed to create "shadows" for aluminum particles that are deposited on the wafer with evaporation process. First, the bottom layer is deposited with an angle of $+45°$. Then, a thin oxide film is deposited homogeneously on the aluminum surface, forming AlOx. Finally, the top layer of the junction is evaporated with an angle of $-45°$, forming a Josephson junction in the region below the Dolan bridge.

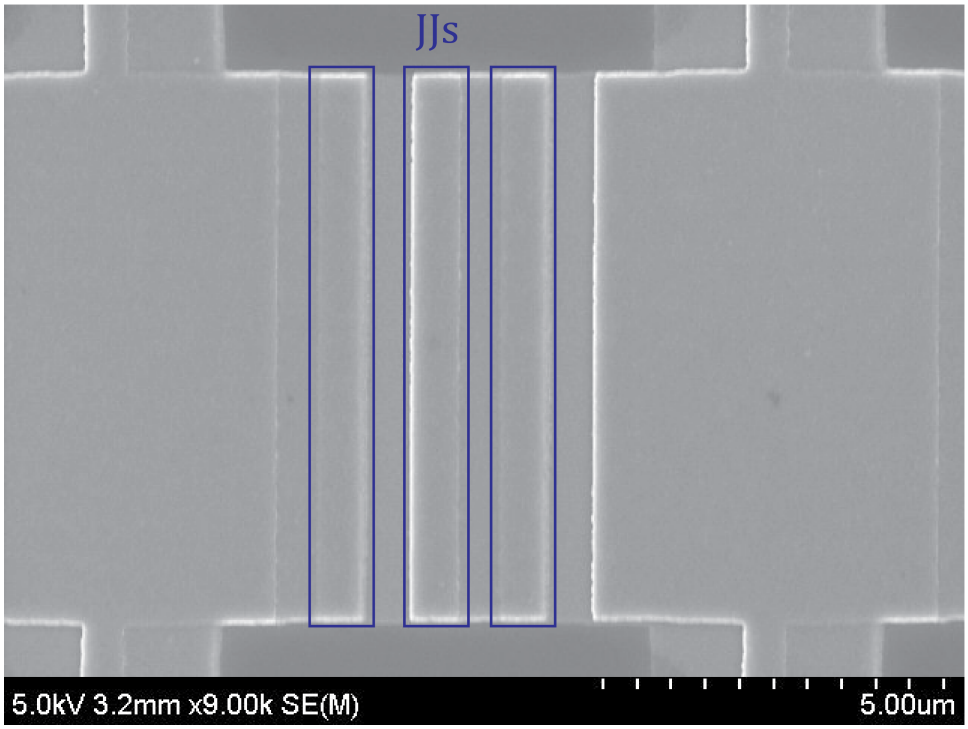

Figure 3.9: SEM image of 3 big JJs forming the central branch of a G-SNAIL. With two Dolan bridges, three JJs can be formed if their geometry and mutual distance are chose correctly. Side junctions area depends on each bridge's area, while center junction area depends on the distance between the bridges.

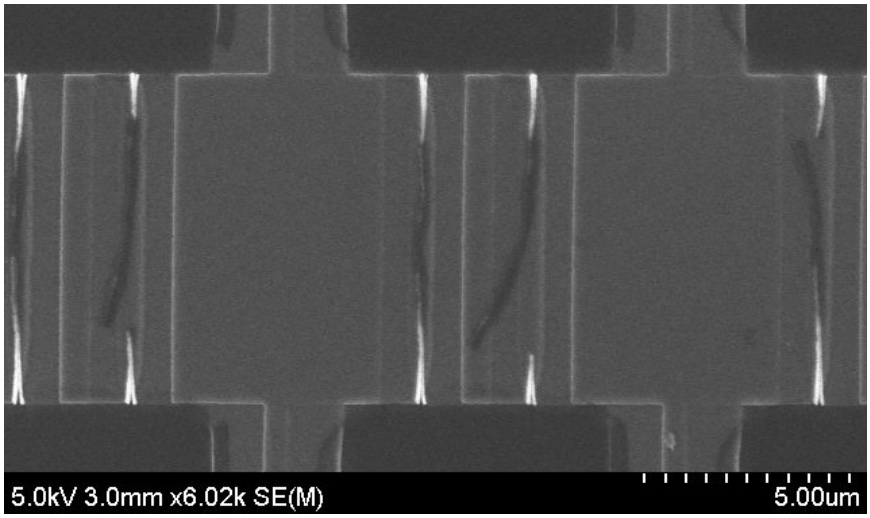

Figure 3.10: SEM image of JJs in the center of a G-SNAIL, deposited with underdeveloped Dolan bridges. The underdevelopment affects the bottom shape of the bridge, that will form a rounded shadow instead of a straight rectangular one. This results in rounded shapes for the sides JJs, while it doesn't affect the shape of the central junction.

upper (walkable) part of the bridge, that is easier to get correctly developed. A SEM image (figure 3.11) of the whole G-SPA shows the placement of the nonlinear array in the microwave resonator, as well as the side flux-lines that are used to tune the coefficients of the implemented Hamiltonian. Each G-SNAIL is composed by three JJs, placed in the center, and two small JJs, shunting on each side. The finished sample is mounted in a copper box with an embedded PCB, in order to provide the required electrical connections for signal, pump and flux-bias ports. The PCB is obtained by milling a Rogers TMM 10 laminate, with a thickness of ≈ 0.3 mm and covered on both sides with a 50 μm thick copper layer. The assembled sample box is shown in picture 3.12 showing signal and pump ports, as well as flux ports where currents are injected into the on-chip flux lines. The flux ports are shunted by 5 Ω resistances, whose role is to provide a low-resistive flow path for bias currents, in case one of them exceeds the critical current of the correspondent flux line. The room temperature resistance of the flux lines was measured to be ≈ 500 Ω each, so the 5 Ω shunts are enough lower to prevent overheating of a flux line in case it switches to normal metal.

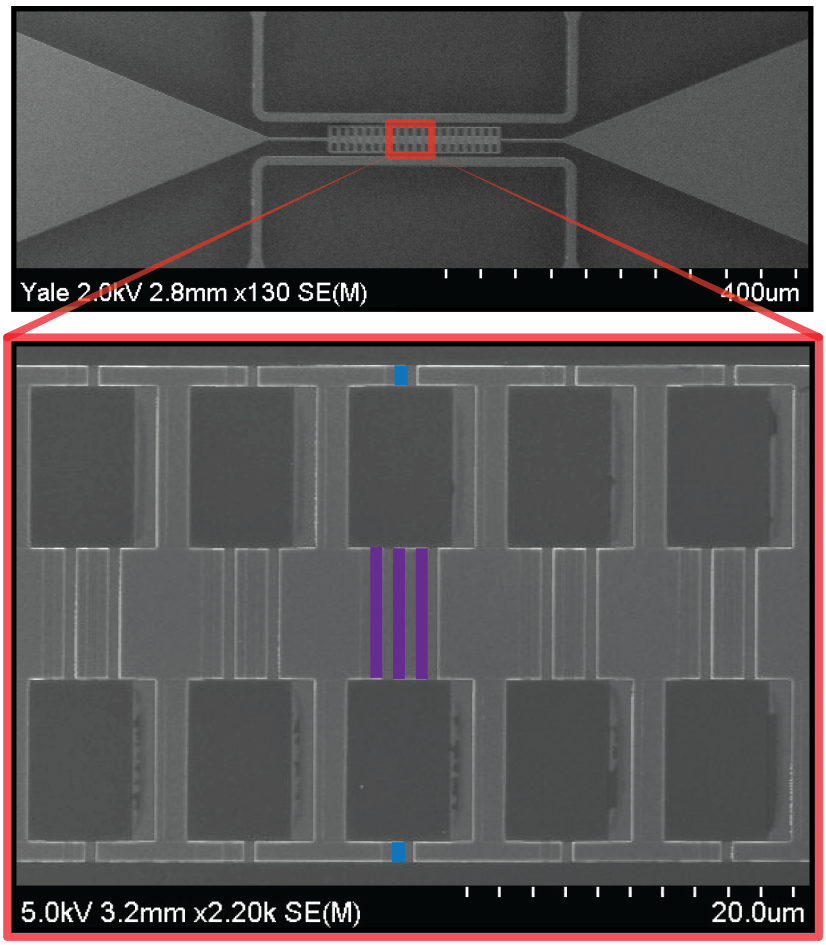

Figure 3.11: SEM image of a Gradiometric SPA. The G-SNAILs array is deposited inside a tapered resonator, with two flux-lines on the sides. Each G-SNAIL has three big JJs (purple) in the middle and one small JJ (blue) per side.

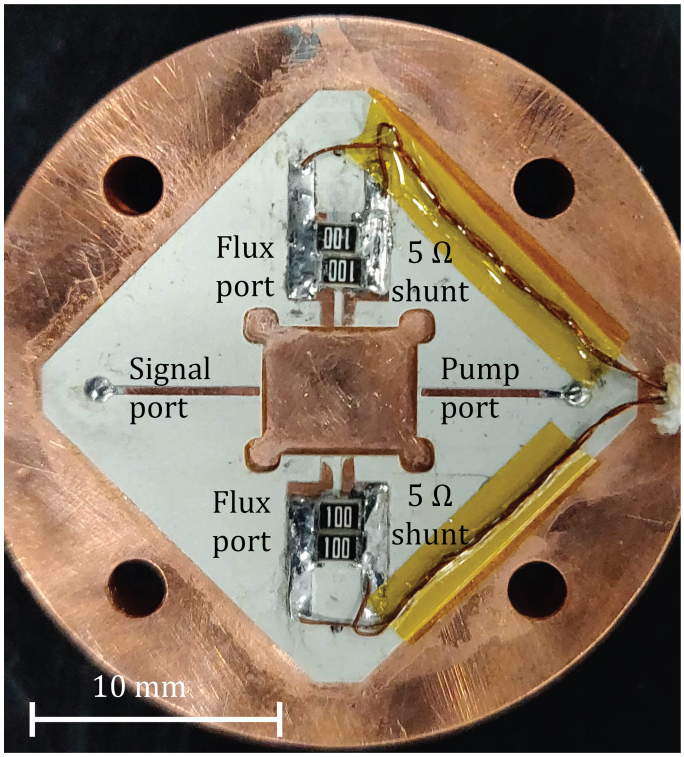

Figure 3.12: Sample holder for a G-SPA. A PCB is glued to a copper holder that hosts SMA connectors on the back (not shown). The PCB is soldered to signal and pump ports of the holder, and has milled copper traces to deliver rf signals and dc bias to the device, that sits in the central slot. Each flux port is resistively shunted by 5 Ω (2 × 10 Ω metallic resistances in parallel) to provide a low-resistance path for the bias currents in case these exceed the critical current of the on-chip aluminum flux lines.

Chapter 4

Experimental methods and results

4.1 Measurement setup

As described in the previous chapters, the characterization of a G-SPA, for both linear and non-linear behaviors, relies on measuring its frequency response under various dc-bias, signal and pump conditions. As the flux-biases need to be independent in order to shape the Hamiltonian with two degrees of freedom, it is necessary to employ two independent generators to current bias the flux lines. With reference to figure 4.1, a current bias is obtained by having a voltage generator with series resistors on each terminal. The DC lines are connected to the G-SPA with twisted pairs in order to reduce magnetic noise pickup, and each line of a twisted pair is connected to the generator with a bias-tee circuit, with the purpose of redirecting any rf signal leakage to a purely reflective load, in this case a short circuit to ground. Despite the twisted pairs were not designed to provide good transmission of rf signals, the amount of measured losses of the device was significantly higher when a bias-tee was not employed to connect the room temperature DC current sources to the DC lines inside the cryostat. The employment of a bias-tee allowed to direct the signal leaked to the flux lines to an RF port at room temperature, decoupling it from the DC instruments employed to provide the flux-bias. By mounting a 50 Ω load on the rf port, higher losses where noticed with respect to the case where a purely reflective short-load was mounted. This suggested that the design needs to be improved in or-

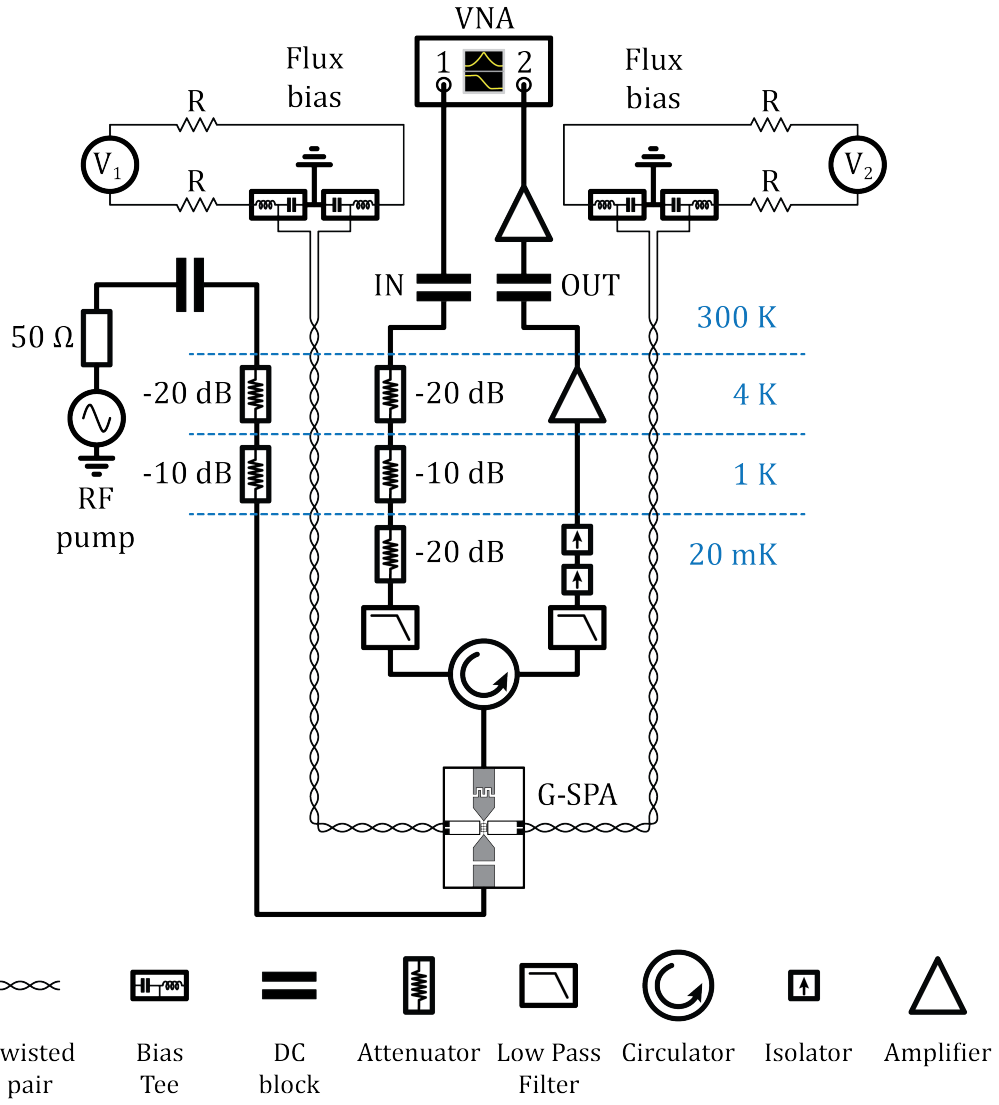

Figure 4.1: Experimental setup for the characterization of a G-SPA. The flux biases are provided by two independent voltage generators with series resistances R, implementing an effective current bias. A VNA is employed to measure the reflection coefficient of the DUT, and an RF pump is delivered with a CW generator.

der to suppress the sensitivity to the electrical environment connected to the flux lines. Regarding the rf side, the G-SPA reflection response was probed through a VNA operated in transmission. All the rf-lines are connected to the instruments with dc-blocks, allowing to galvanically separate cryostat ground from the rest of the setup. This is particularly useful in order to have a control of how the grounds are connected and, in general, to avoid wild ground loops that can harm the noise properties of the measurements. By using a circulator, it was possible to physically separate incident and reflected microwave signals on the Device Under Test (DUT), in order to have a different setup for input and output lines. In fact, it is necessary to employ a chain of cold attenuators on the input lines, in order to obtain a reasonable signal-to-noise ratio. In this way it is possible to reach the required low power at G-SPA signal port by starting with an high power at room temperature. This allows to inject an high SNR signal in the input line, that is then attenuated by cryogenic attenuators. These ones, being at low temperatures, add a much lower amount of thermal noise $\propto k_B T$ with respect to an attenuator placed at room temperature. Input line is then low-pass filtered with a cutoff at 12 GHz for noise performance purposes. On the output line, an additional low pass filter is put in order to cut pump modes that usually are applied at twice the resonance frequency of the device. Then, a chain of two rf isolators are put after the LPF in order to shield the device from a cold HEMT amplifier sitting on the 4K plate. This latter is employed as a first, low noise preamplification stage in order to raise the signal level above enough the VNA receiver noise floor. Then, output signal is further amplified at room temperature and finally reaches the VNA receiver. Last, an RF pump can be applied to the G-SPA, for example, to excite three-wave mixing operations. The pump is generated with an rf CW generator, and is attenuated at cold stages of about -30 dB. The less attenuation of the pump with respect to the signal comes mainly from two reasons: first, the pump needs to be strong enough in order to excite the desired nonlinearities in the G-SPA and, secondly, the pump port is very weakly coupled in order to avoid significant signal leakage out of it.

4.2 Experimental data

In this section, experimental data will be discussed, showing the advanced Hamiltonian tuning capabilities of the G-SPA. The possibility of keeping Kerr

suppressed at different operating frequencies and, at the same time, exciting 3WM operations will be presented. First, linear response measurements at low signal power will be shown in order to characterize the resonance frequency as a function of both φ_+ and φ_- bias phases. This provides important information about the flux tunability, frequency operating range, internal and coupling losses of the device. A comparison with numerical simulations will be made in order to validate the design experimental parameters. Then, the nonlinear response of the G-SPA will be acquired by measuring the resonance frequency as a function of the bias phases, while at the same time, sweeping the input signal power in order to show the Stark shift of the resonance frequency. This allows to individuate a 1-D region where the Kerr is suppressed, namely a Kerr-free line, along which the operating frequency of the G-SPA can be chosen. It will also be shown that it is possible to obtain 20 dB amplification by applying a pump at twice the resonance frequency on Kerr-free points, demonstrating that the device can implement Kerr-free three-wave mixing operations for different linear responses.

4.2.1 Resonance frequency

To characterize the linear response of the device, the complex reflection coefficient at signal port $S_{11}(\omega)$ of the G-SPA is measured as a function of φ_+ and φ_-. For a given combination of dc-flux biases, the resulting S_{11} curve is fitted to the model of a damped resonator capacitively coupled to a microwave generator. The fit is performed with the "resonator tool fit" program [43], that has the capability of algebraically fitting the complex function $S_{11}(\omega)$ without the need of iterative processes that can have convergence issues when data is noisy and the initial guesses of parameters aren't in the vicinity of the experimental ones. The phase of reflected wave at G-SPA signal port is shown in figure 4.2 as a function of probe tone frequency $\omega/2\pi$, common-mode bias flux φ_+ and for a fixed value of differential flux-bias $\varphi_-/2\pi = 0.63$. A fit of the resonance frequency, performed through the above mentioned code for each value of φ_+, is superimposed on the measured data with white markers, to have a direct visual comparison of the two. Overall, the fit data is in very good agreement with the measured data. In order to have a complete visualization of the resonance frequency landscape as a function of both bias fluxes, the fit procedure is replicated also for each value of φ_-. This turns to be an experimental characterization of the function $\omega(\varphi_+, \varphi_-)$, characterizing the linear part of G-SPA Hamiltonian (2.31). The measured resonance

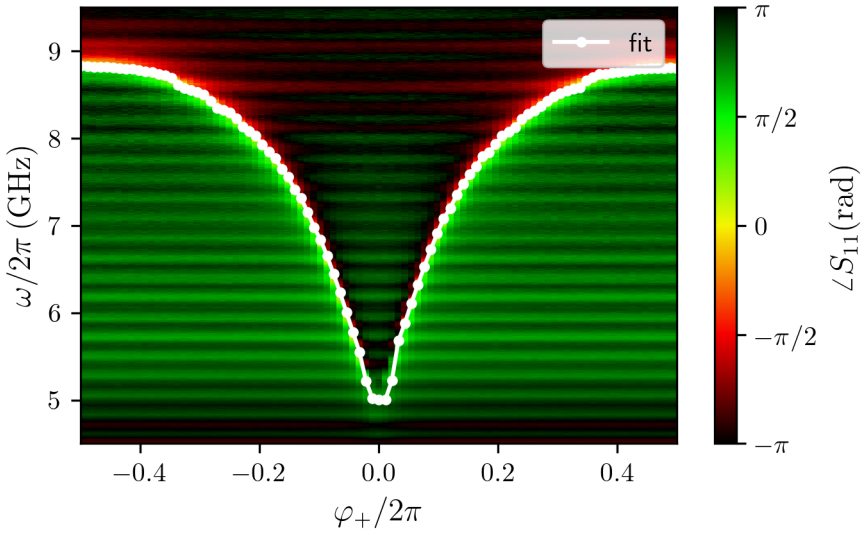

Figure 4.2: Measured phase of reflection coefficient S_{11} of the experimental device as a function of frequency $\omega/2\pi$ and bias flux φ_+, for a fixed value of $\varphi_-/2\pi = 0.63$. For each value of φ_+, the resonance is extracted by a fit procedure that returns the value of resonance frequency (white markers).

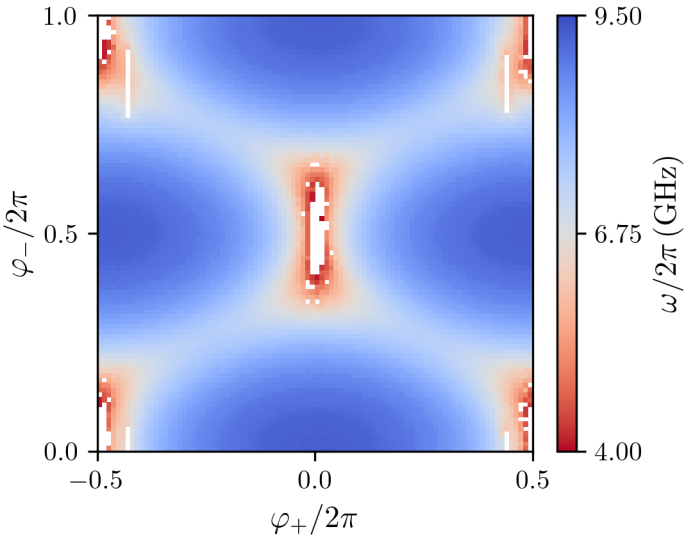

Figure 4.3: Measured resonance frequency. The white regions represent flux points where the resonance was outside the acquisition range of the microwave setup. A whole period in both φ_- and φ_+ fluxes is represented.

frequency can then be plotted as a function of the two bias fluxes, as in figure 4.3, where horizontal and vertical axes are, respectively, bias phases φ_+ and φ_-, with the color representing the value of resonance frequency. In this plot, both bias phases show a whole flux quantum tunability, and the resonance frequency appears to satisfy the relation $\omega(\varphi_+ \pm n\pi, \varphi_- \pm n\pi) = \omega(\varphi_+, \varphi_-)$, as expected from the model presented in chapter 2. Data from this figure can then be compared to simulated resonance frequency, in order to obtain an estimate of the design parameters of the experimental device. By selecting a large enough portion of the experimental data where there are no holes because of missing points, a nonlinear least-square fit algorithm is employed in order to extract best fit values for the geometrical parameters of the G-SPA. Figure 4.4 shows a comparison between measured resonance frequency and simulated one. The simulation is performed with the following set of best-fit parameters

α	L_j	Z_0	$\omega_0/2\pi$
0.145	27 pH	50 Ω	15.6 GHz

where Z_0 has been pre-selected to 50 Ω and all the other ones were kept free

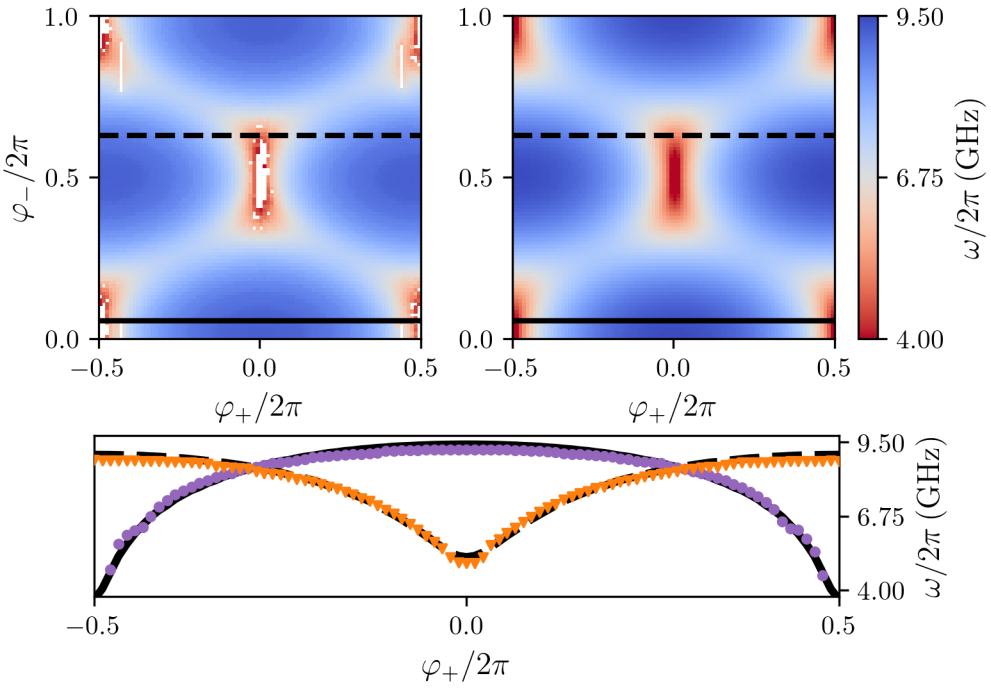

Figure 4.4: Comparison between experimental data and simulated data for the resonance frequency of a G-SPA. Simulated data is obtained with a set of design parameters extracted with a least-square fit to measured data. Experimental and simulated resonance frequency curves are compared for two values of differential bias phase φ_-, showing quantitative agreement.

to vary in an acceptable range around the expected design values.

4.2.2 Kerr-free lines

As explained in the second chapter, the nonlinear response of a G-SPA is produced by the coefficients g_3 and g_4 of the Hamiltonian (2.31). While the three-wave mixing operation only depends on third order nonlinearity g_3, the detrimental Kerr effect is a function of all the expansion coefficients of the Hamiltonian. In order to characterize the Kerr, it is possible to measure the resonance frequency Stark shift as a function of the population of the resonator. In fact, the Stark shift detuning Δ is directly related to the Kerr, when evaluated for a not-too-crowded resonator, being $\Delta = K\bar{n}$. For the following analysis, it is useful to introduce the coefficient $R(\varphi_+, \varphi_-) = \bar{n}/P_{\text{in}}$ that relates the number of photons in the resonator with the input power at signal port. The functional form of R is well known from linear resonators theory

$$R = \frac{4k_c}{2\pi\hbar\omega\left(k_c + k_i\right)^2} \tag{4.1}$$

and it is an always-positive function that depends on resonance frequency, internal and coupling bandwidths k_i and k_c. Then, Stark shift can be directly related to input signal power as

$$\Delta = RKP_{\text{in}} = B(\varphi_+, \varphi_-)P_{\text{in}}. \tag{4.2}$$

The B coefficient, then, carries the signature of the Kerr, as $\text{sign}(B) = \text{sign}(K)$ and $B = 0 \leftrightarrow K = 0$, being $R > 0 \ \forall \ (\varphi_+, \varphi_-)$. Notice that, from an experimental point of view, points where $B \approx 0$ because the R coefficient is very small (possible if strong internal losses are present), can still be distinguished from Kerr-free points where $K \approx 0$. In fact, while R cannot change sign, Kerr coefficient will become zero in correspondence of a change of sign, that will reflect in a change of sign of B. A first experimental characterization of resonance frequency Stark shift is shown in figure 4.5, where, for a fixed value of differential phase bias $\varphi_- = 0.33$, corresponding to a value of $\alpha_{\text{eff}} = 0.139$, a signal power sweep is performed for three different values of φ_+. The phase of S_{11} coefficient is presented in order to identify the position of the resonance. In the first plot, for $\varphi_+ = -0.13$, a negative detuning can be seen, as the resonance frequency decreases while increasing the pump power. On the other hand, for $\varphi_+ = 0.04$, a positive Stark shift is

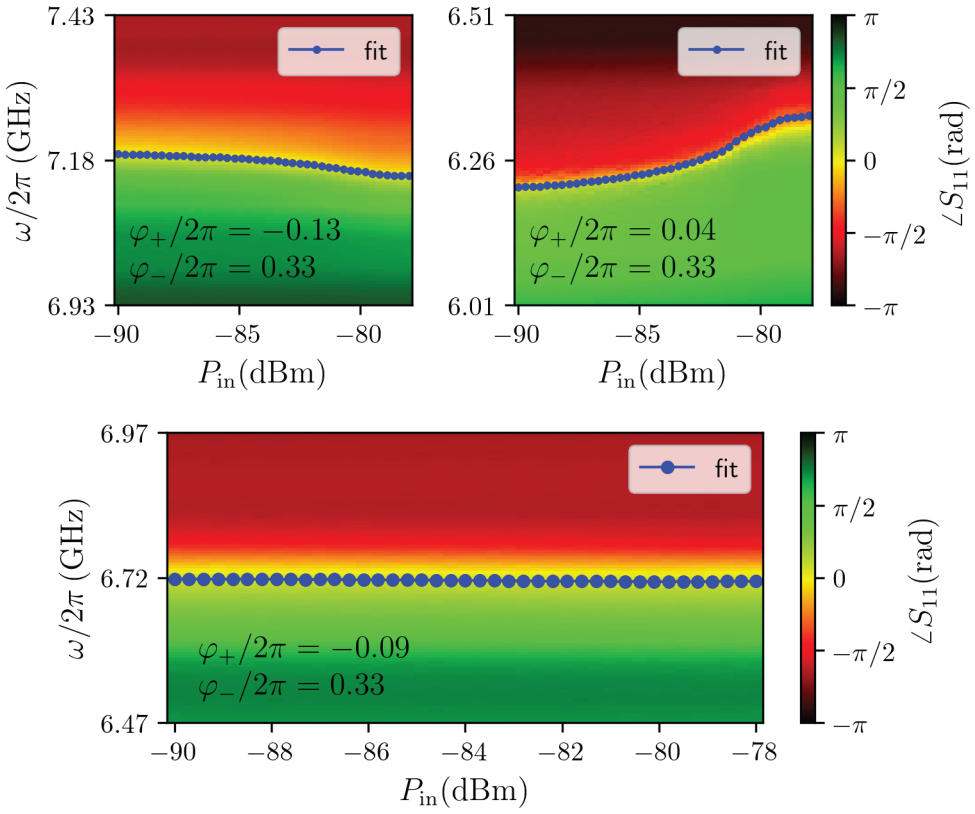

Figure 4.5: Measured $\angle S_{11}$ for fixed values of φ_+ and φ_-, as a function of input signal power P_{in}. With a fixed value of $\varphi_-/2\pi = 0.33$, for different values of φ_+ it is possible to have negative Stark shifts (fig.a), positive Stark shifts (fig.b) or strongly suppressed Stark shifts (fig. c). Flux points in fig.c identify a Kerr-free point, where the resonance frequency of the G-SPA does not depend, at least for low powers, on the photons occupation of the cavity. Notice how a Kerr-free point corresponds to a fixed value of resonance frequency.

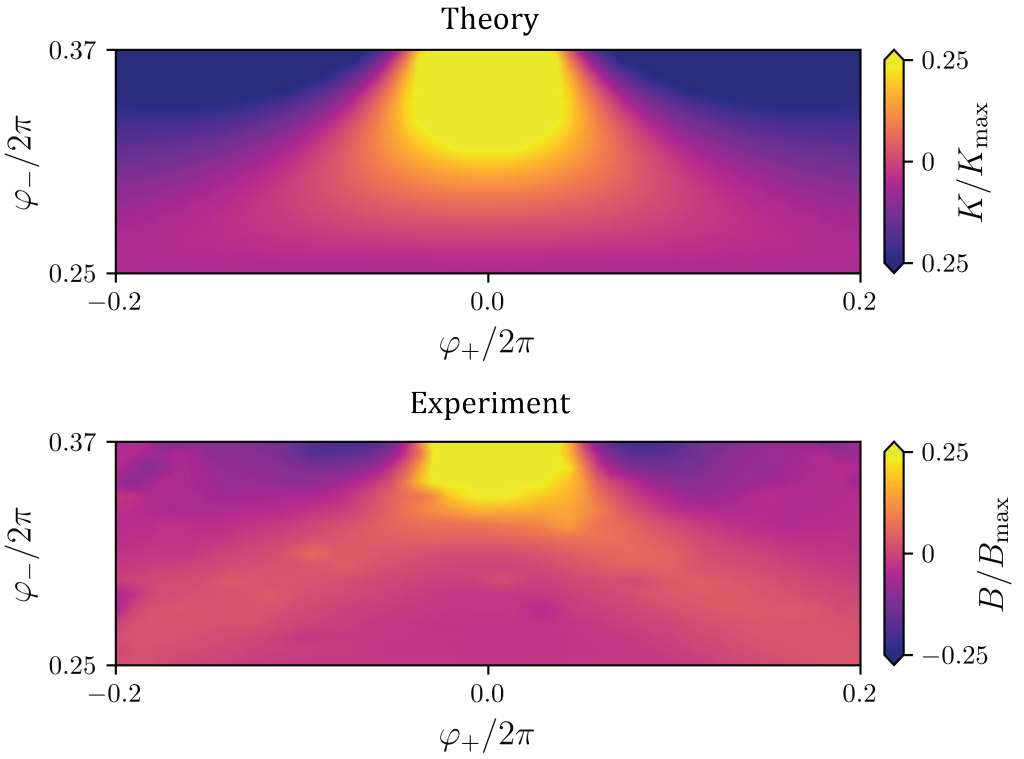

Figure 4.6: Kerr extracted from simulations in comparison with experimentally measuered B. The model employed correctly guesses the region of fluxes where Kerr-free points are present. A qualitative prediction can be made by the model.

obtained. These two plots refer, respectively, to negative and positive values of B, i.e. negative and positive values of K. In the third plot, for $\varphi_+ = -0.09$, the Stark shift is strongly suppressed, as the resonance frequency is almost independent of the signal input power: this behavior identifies a Kerr-free point, where $K \approx 0$. The resonance frequency value is extracted with the previously mentioned fit tool for resonators, and it is in pretty good agreement with the experimental data. With the experimental sampling of the Stark shift frequency detuning in figure 4.5, it is now possible to experimentally evaluate the B coefficient. This is done with a least square fit of a first order polynomial to the resonance frequency data extracted while sweeping bias phases φ_+ and φ_-, as well as signal input power P_{in}. The angular coefficient of this polynomial is then identified as B. In figure 4.6, the experimentally measured B coefficient is compared to simulated Kerr K

in a region where the Stark shift is significantly present. The two quantities are normalized to their respective maximum values in the bias phases region of interest, $B_{\max} = 64\ \frac{\text{Mhz}}{\text{pW}}$ and $K_{\max} = 2 \times 10^{-3} E_C/\hbar$ respectively. The two plots show a good qualitative agreement, and it is possible to identify corresponding regions where the detuning is positive or negative, with the same trend in both theory Kerr K and experimental B. The main difference between the extracted B and the simulated Kerr is in the bottom inner region of the plots. A better insight in this is provided by a plotting the absolute values of the two quantities, in order to easily identify the Kerr-free lines. The absolute values plots of figure 4.6 are represented in figure 4.7, where KFLs appear as dark blue regions. Comparing the simulated KFLs with the measured ones, it is possible to see a difference in shape in the same region of bias phases. Despite the difference in shape, theory correctly predicts the region of fluxes where the KFLs appear in the experimental device, confirming a qualitative agreement between theory and experiment. The main difference between the two plots is in the lower half region of the φ_- axis, where experimental lines appear more spread than what is predicted by theory. For high values of φ_-, instead, the position of the lines is more consistent between the two plots. Possible explanations for this discrepancy can come from different considerations. To exclude fitting artifact, in figure 4.8, Stark shift measured data is plotted for three different values of φ_+, while keeping $\varphi_-/2\pi = 0.27$ ($\alpha_{\text{eff}} = 0.036$), in order to cross the distorted KFL from side to side. From these plots, it is possible to identify a change of sign of the detuning as one moves from point **a** to point **c**. This trend identifies the presence of a Kerr-free point, in correspondence of the crossing of the distorted KFL. The exclusion of fitting artifacts can move the question about the origin of the mismatch between theory and experiment to the device and/or the theory model. The numerical simulations of the Kerr were performed through a model introduced in [21], where the Kerr is corrected by a second order perturbation theory contribute from g_3, as explained in chapter 2. This correction allowed to quantitatively predict the position of Kerr-free points in standard SPAs, also for different values of α. Because the G-SPA effectively behaves as a SPA with a tunable α via the differential bias flux φ_-, it should be possible, with the same model for and SPA, to predict its Kerr-free points quantitatively as a function of both bias fluxes φ_+ and φ_-. The main discrepancy between the theory predicted Kerr-free lines and measured ones is more evident as the value of α_{eff} approaches zero. This region corresponds to a strong effect of the additional bias term φ_- in the

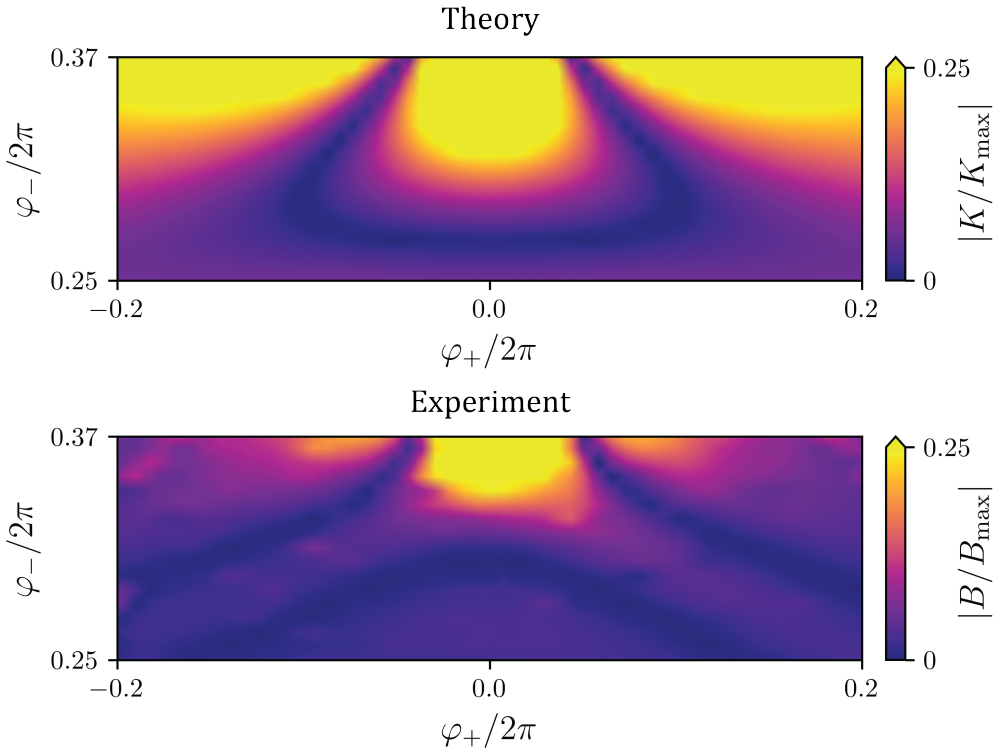

Figure 4.7: Absolute values of simulated Kerr and experimentally extracted B coefficient. The dark blue regions identify Kerr-free lines. With respect to the simulated Kerr, the experimentally evaluated Kerr-free lines appear distorted. The region of bias fluxes where the experimental KFLs are present is in agreement with what predicted by theory.

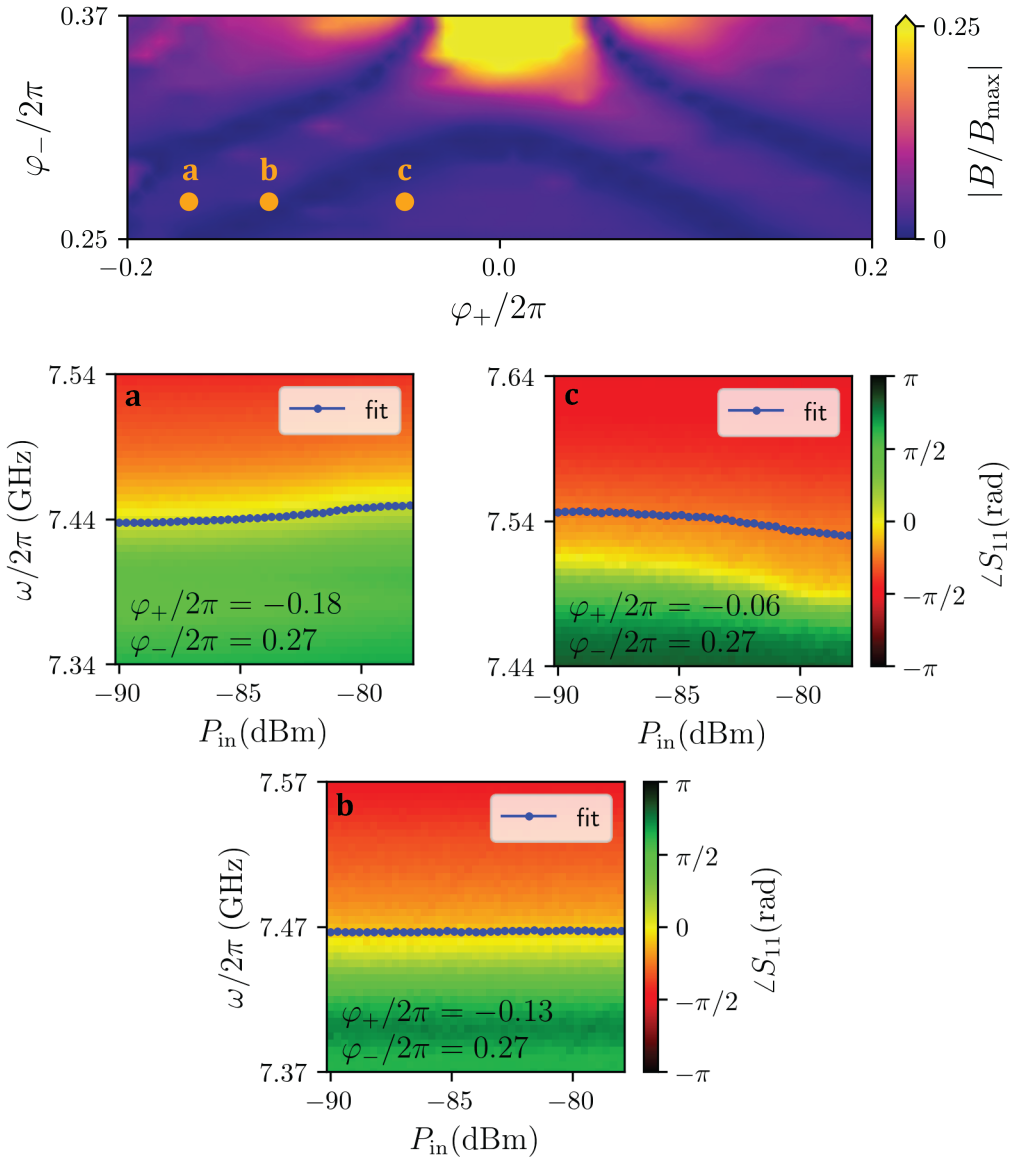

Figure 4.8: Stark shift measurements for three different values of φ_+, selected in order to evaluate the validity of the distorted Kerr-free lines. Plot **a** and plot c, selected on the left and on the right of the distorted Kerr-free line, show, respectively, negative and positive Stark shifts. The **b** point, in the most vicinity of the KFL, shows suppressed Kerr. Fit resonance frequency reflects correctly the sign of the detuning, also when an offset is present as in figure **c**.

cancellation of the nonlinear contributions from the two small JJs on the sides of each of the G-SNAILs forming the array. It is reasonable to expect that inhomogeneities in the array that can arise from fabrication imperfections can affect the behavior of higher order effects, as Kerr. Imperfections can be present inside each G-SNAIL where, for example, the three big junctions in the center, supposed identical, can result different because of fabrication uncertainties, changing the effective shape of the potential energy function of each elementary cell. As the deviation from what predicted by theory is clearly noticeable when $\varphi_-/2\pi < 0.3$, corresponding to $\alpha_{\text{eff}} < 0.1$, it is possible that some asymmetries between the two small junctions in the array are causing the discrepancy between experiments and simulations. In fact, the cancellation of α_{eff} requires the small side junctions of each G-SNAIL to be perfectly identical. Moreover, it is difficult to ensure perfectly developed bridges all along the structure while writing the mask with the e-beam, as proximity effect is more present in the center of the array than on its sides. This can produce lower I_c than expected for the junctions at the sides of the array, changing the contribution of the corresponding cells in the overall potential energy (2.27). A numerical analysis, based on the model presented and taking into account these types of imperfections of the G-SPA, is in progress in order to understand if they can give rise to distorted Kerr-free lines. Also, to exclude that the distortion is not predicted by a more sophisticated theory, full quantum simulations with QuTiP software [44] are in progress, where the energy spectrum $E(n)$ of the G-SPA can be directly computed from a full Hamiltonian, expressed up to a desired order, and Kerr computed as from definition, d^2E/dn^2. These two analyses should contribute to advances in the understanding of the design and fabrication accuracy required in order to produce devices that quantitatively agree with their theoretical model. It will also be possible to have an hint on if purpose-designed asymmetries can actually give beneficial effects on the nonlinear behaviors of these superconducting circuits. These could be designed, for instance, to shape Kerr-free lines in such a way to enhance the frequency tunability along them.

4.2.3 Kerr-free three wave mixing and frequency tunability

The presence of Kerr-free lines has a strong impact on the types of Hamiltonians that a G-SPA can implement. In fact, by selecting phase biases points that belong to these sweet spots, it is possible to tune some other parameters as, for instance, the device operating frequency, while still keeping Kerr-free operation mode. Moreover, the three-wave mixing coefficient g_3 is usually non-zero on Kerr-free points, meaning that it is in principle possible to operate a G-SPA as a Kerr-free parametric amplifier at different resonance frequencies. In order to demonstrate these advanced tuning capabilities of a G-SPA, gain curves have been experimentally measured on Kerr-free points that correspond to different operating frequencies, as shown in figure 4.9. This figure shows experimental data of Stark-shifted resonance frequency for two values of φ_-, while sweeping φ_+ and input signal power P_{in}. On the top-left panel, for $\varphi_- = 0.33$, resonance frequency curves are plotted as a function of φ_+, on the horizontal axis, while the color of each curve represents the corresponding value of input signal power P_{in}. Notice that there are points where the curves intersect each other meaning that, in their correspondence, the resonance frequency does not change with the applied input signal power. These points are Kerr-free points, as also evident from the plot of B in the center-left panel, that crosses zero in their correspondence. To demonstrate that three-wave mixing is possible in these sweet-spots, a gain curve is acquired in a Kerr-free point, by applying a pump tone at a frequency $\omega_p = 2\omega$, in order to excite a degenerate parametric gain. The bottom-left panel shows that is in fact possible to obtain a 20 dB gain at the $\omega/2\pi = 6.76$ GHz, corresponding to the frequency of the Kerr-free point for $\varphi_- = 0.33$, i.e. $\alpha_{\text{eff}} = 0.139$. This behavior is already well known in parametric amplifiers based on standard SNAILs [21,22], but these are also limited to present such a feature for a single value of resonance frequency only. A G-SPA, instead, can make good use of the additional phase bias knob φ_-, whose choice can change the position of a Kerr-free point, along a Kerr-free line, making it correspond to a different value of operating frequency ω. In fact, the right panels of figure 4.9 show the same feature of Kerr-free three-wave mixing amplification, but for a different value of differential bias phase $\varphi_- = 0.38$, corresponding to a value of $= 0.21$. This time, the Kerr-free point appears for a resonance frequency of $\omega/2\pi = 5.87$ GHz, about 1 GHz away from the Kerr-free resonance for $\varphi_- = 0.33$. Moreover, this Kerr-free point can be

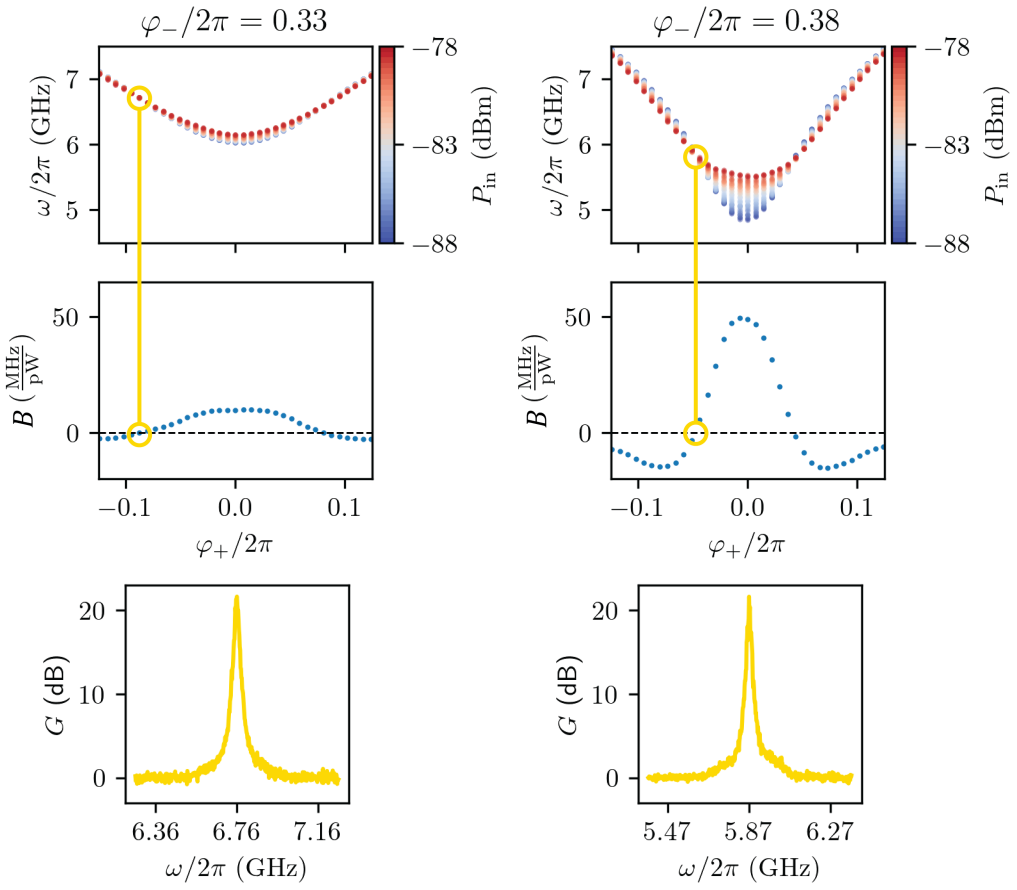

Figure 4.9: Stark shift measurements. The resonance frequency is acquired as a function of bias phases φ_+ and φ_-, while sweeping input signal power P_{in}. The B coefficient is directly proportional to Kerr and, when zero, identifies a Kerr-free point. Plots for different values of φ_- show that is possible to change the position of a Kerr-free point in order to make it correspond to different values of resonance frequency.

pumped in order to produce a 20 dB gain curve, again with $\omega_p = 2\omega$. This last figure demonstrates the advanced Hamiltonian-tuning capability that is achievable with a G-SPA. In fact, it proves that two flux-bias knobs can provide enough flexibility to eliminate an unwanted nonlinear effect as the Kerr and, at the same, can freely tune one of the other Hamiltonian parameters to the desired working point. The cancellation of the Kerr requires a precise balance of nonlinear expansion coefficients of the G-SPA c_2, c_3 and c_4, as explained in the second chapter, while the resonance frequency only depends on c_2. Then, the Kerr cancellation for different values of resonance frequency, i.e. different values of c_2, is a process that requires the zeroing of a complex function of the G-SPA expansion coefficients such that, for any value of c_2, c_3 and c_4 are correctly weighted resulting in $K = 0$. This behavior is very desirable when precise, Kerr-free amplification is required for the readout of a superconducting qubit, with the additional feature of being able to operate selectively at different frequencies. In fact, with a single G-SPA, many detuned qubits, operating at different frequencies, can be read while keeping the device tuned to a sweet-spot where the Kerr nonlinearity is suppressed. This peculiarity of the G-SPA arises from the two tuning degrees of freedom of the potential energy function implemented by the G-SNAILs, providing advanced tuning capabilities of the Hamiltonian of the circuit in which are embedded. More in general, G-SNAILs can benefit many applications that are nowadays constrained by the presence of parasitic effects arising from residual nonlinearities in the Hamiltonians of the employed devices.

Chapter 5

Perspectives and conclusion

5.1 Perspectives

5.1.1 Facilitate parametric interactions between superconducting cavities

Superconducting 3D cavities are lead actors in bosonic quantum information processing, where the two level systems employed as qubits are isolated from linear, very high Q superconducting cavities entirely made of aluminum. A nonlinear element as a transmon is usually coupled to these cavities in order to make them readable, providing the required anharmonicity that allow to discriminate between the two states. In many applications, two or more cavities are employed with different roles [12, 19, 29] and their interaction is mediated by on-demand activated parametric processes. When the involved process is 3WM, as described in the first chapter, it could be important to suppress the Kerr to have very high fidelity in converting photons from a cavity to another. In this frame, the device presented in this manuscript could be of great help, facilitating the synthesis of precise Hamiltonians that implement pure, tunable parametric processes to mediate coherent energy exchange between multiple cavities in a quantum processor.

5.1.2 Implementations with ferromagnetic Josephson junctions

Recently, unconventional Josephson junctions where a thin, ferromagnetic layer is deposited as a part of the tunnel barrier, have been experimentally demonstrated as capable of macroscopic quantum tunneling, when operated below a certain temperature. From a fundamental physics perspective, this result is quite remarkable as ferromagnetism and superconductivity are two aspect that were supposed incompatible in the beginning. Instead, if the ferromagnetic layer is fabricated with thickness smaller than the London penetration depth of the superconductors that form the metal leads of the JJ, the Cooper pairs are capable of tunneling through it without breaking, thus preserving the superconducting transport properties of standard Josephson junctions. This suggests that these junctions can be employed in superconducting quantum circuits, where their peculiar nonlinear behaviors can be of interest for designing new types of tunable interactions. In fact, the presence of a ferromagnetic layer inside the junction can behave as a magnetic memory that directly reflects in the critical current value of the device [45–48]. Such a behavior can be practical in many applications where, instead of a continuous, analog tuning of the microwave response of the junctions in a superconducting device, it is more suited to have just two possible behaviors. This "digital" control of ferroMagnetic Josephson Junctions (MJJs) critical currents is directly related to the hysteresis of the $M(H)$ magnetization function of the particular employed ferromagnet, and the switch between the two selected stable states is easily obtained by applying single magnetic pulses to the device. An MJJ would then implement a potential energy term of the form

$$U_{\mathrm{MJJ}} = E_{\mathrm{MJJ}}(\Phi_{\perp}) \cos\varphi \tag{5.1}$$

where $E_{\mathrm{MJJ}}(\Phi_{\perp})$ is the MJJ Josephson energy that can be tuned with a magnetic flux $\Phi_{\perp}$ orthogonal to the current flow direction. This type of junction can have an hysteretical behavior in $\Phi_{\perp}$, depending on the ferromagnet present in the barrier. An interesting application could be to implement a SNAIL with an MJJ junction shunted by an array of 3 traditional SIS JJs, such that all their Josephson energies can be tuned with an orthogonal flux. The presence of an MJJ in the loop could heavily distinguish the tunability in $\Phi_{\perp}$ of the MJJ from the one of the SIS JJs, in order to have a desired behavior. Moreover, while an SIS junction with no orthogonal flux will have

the maximum critical current, an MJJ will have a critical current lower than the maximum as a consequence of the possible residual magnetization of the embedded ferromagnet.

MJJs are also capable of implementing π junctions [49, 50], where the typical $i(\varphi)$ of a standard Josephson junction is phase-shifted as it appears as $i_\pi(\varphi) = I_c \sin(\varphi - \pi)$. Moreover, these unconventional junctions can implement current-phase responses that have also additional terms with respect to the standard $\sin\varphi$ one, where higher harmonics are present that change the usual shape of tunnel Josephson junctions potential energy function. In particular, the presence of a second harmonic in the $i(\varphi)$ relation of Superconductor-Ferromagnet-Superconductor junctions has been experimentally demonstrated [51] and can provide additional freedom in the accurate and flexible synthesis of parametric processes, with proper design choices. Based on these recent advances, it would be of particular interest to understand the novel features that a superconducting device based on JJs and various types of MJJs can deliver into the superconducting quantum information processing field.

5.2 Conclusion

This manuscript presented the first experimental proof-of-principle of the advantages that a double-flux-biased superconducting circuit can provide in terms of tuning of its Hamiltonian parameters. With two bias degrees of freedom, it was possible to implement Kerr-free, 20 dB parametric amplification for different values of resonance frequency, that can be chosen over a continuum with a span of more than 1 GHz. Such a result opens to many possible applications, and makes the G-SNAIL a very promising hardware component for implementing precise control circuitry for the weak coherent microwave signals employed in superconducting quantum information processing.

The measured data shown in chapter 4 demonstrated that the concept of Kerr-free lines has an experimental counterpart. The measured KFLs are distorted with respect to the theory predictions, but the region of bias fluxes where they appear is correctly predicted by the model. This discrepancy is currently under investigation from both theory and experimental sides, in order to understand its origin. More sophisticated numerical simulations are being performed, where the Kerr is directly extracted from a full quantum analysis with QuTiP software [44]. Moreover, an optimized G-SPA device

is currently in fabrication in an industrial-grade facility, where the flux lines have been engineered in order to not provide internal losses, and the design as well will have a very high level of homogeneity of the elementary G-SNAIL cells. Aside from the application for Kerr-free three-wave mixing at different frequencies, the G-SPA would be practical whenever a contemporaneous tuning of two Hamiltonian parameters is desired. This enhanced tuning can be beneficial for both flexibility and to have an advanced, precision control for design-critical applications where is not feasible to hit the required value of a parameter, for example the α of a SNAIL, at the design level. In fact, a G-SNAIL, implements a tunable $\alpha_{\text{eff}} = 2\alpha \cos \varphi_-$ that can be controlled with a precision that is only limited by the accuracy of the DC sources employed to provide the bias fluxes.

An immediate application of the G-SPA would be the capability to readout multiple qubits, operating at different frequencies, with Kerr-free 3WM. Kerr-free operation allows to amplify high power microwave signals without distortion, enabling to probe a resonator that host the qubits with multiple photons in order to enhance readout speed and fidelity. The G-SNAIL is also a very good candidate to implement a 3WM TWPA with high performances. In fact, thanks to the capability of tuning the linear response while changing the efficiency of higher order processes, this device can be fine-tuned to provide the correct characteristic impedance to a TWPA and, at the same time, tune 3 and 4 photons processes in order to produce large bandwidth gain profiles. The gain of a 3WM TWPA, in fact, is highly sensitive to 4 photons processes, that are capable of "breaking" the phase locking required between signal, idler and pump tones in order to produce 20dB gain on a bandwidth of many GHz [14]. The G-SNAIL can also be employed to drive fine-tuned parametric interactions between two superconducting cavities, where the two bias degrees of freedom can be used to implement tailor-made Hamiltonians not containing unwanted terms that can harm the efficiency of a desired operation. In fact, if a beam-splitter interaction between two cavities is mediated by a circuit implementing a 3WM process, the presence of a residual Kerr in its Hamiltonian can be harmful for the effectiveness of the operation.

In general, G-SNAILs can provide many benefits to any GHz operation with superconducting circuits, in particular when a device is required to implement an Hamiltonian that is as close as possible to an ideal one. In applications where only one interaction is predominant and the residual effects need to be suppressed as much as possible, a G-SNAIL would be a perfect choice. With just a little added technological complexity with respect

to a SNAIL, in order to provide two on-chip flux biases, the Gradiometric-SNAIL can be easily integrated in all the superconducting devices powered by SNAILs, increasing their tuning capabilities and broadening their range of applications.

Bibliography

[1] J. Koch, T. M. Yu, J. Gambetta, A. A. Houck, D. I. Schuster, J. Majer, A. Blais, M. H. Devoret, S. M. Girvin, and R. J. Schoelkopf, "Charge-insensitive qubit design derived from the Cooper pair box", *Physical Review A*, vol. 76, no. 4, p. 042319, Oct. 2007.

[2] J. A. Schreier, A. A. Houck, J. Koch, D. I. Schuster, B. R. Johnson, J. M. Chow, J. M. Gambetta, J. Majer, L. Frunzio, M. H. Devoret, S. M. Girvin, and R. J. Schoelkopf, "Suppressing charge noise decoherence in superconducting charge qubits", *Physical Review B*, vol. 77, no. 18, p. 180502, May 2008.

[3] A. Blais, R.-S. Huang, A. Wallraff, S. M. Girvin, and R. J. Schoelkopf, "Cavity quantum electrodynamics for superconducting electrical circuits: An architecture for quantum computation", *Physical Review A*, vol. 69, no. 6, p. 062320, Jun. 2004.

[4] A. Wallraff, D. I. Schuster, A. Blais, L. Frunzio, R.-S. Huang, J. Majer, S. Kumar, S. M. Girvin, and R. J. Schoelkopf, "Strong coupling of a single photon to a superconducting qubit using circuit quantum electrodynamics", *Nature*, vol. 431, no. 7005, pp. 162–167, Sep. 2004.

[5] B. Abdo, K. Sliwa, S. Shankar, M. Hatridge, L. Frunzio, R. Schoelkopf, and M. Devoret, "Josephson Directional Amplifier for Quantum Measurement of Superconducting Circuits", *Physical Review Letters*, vol. 112, no. 16, p. 167701, Apr. 2014.

[6] B. Abdo, A. Kamal, and M. Devoret, "Nondegenerate three-wave mixing with the Josephson ring modulator", *Physical Review B*, vol. 87, no. 1, p. 014508, Jan. 2013.

[7] N. Bergeal, R. Vijay, V. E. Manucharyan, I. Siddiqi, R. J. Schoelkopf, S. M. Girvin, and M. H. Devoret, "Analog information processing at the quantum limit with a Josephson ring modulator", *Nature Physics*, vol. 6, no. 4, pp. 296–302, Apr. 2010.

[8] T.-C. Chien, O. Lanes, C. Liu, X. Cao, P. Lu, S. Motz, G. Liu, D. Pekker, and M. Hatridge, "Multiparametric amplification and qubit measurement with a Kerr-free Josephson ring modulator", *Physical Review A*, vol. 101, no. 4, p. 042336, Apr. 2020.

[9] A. Metelmann and A. A. Clerk, "Quantum-Limited Amplification via Reservoir Engineering", *Physical Review Letters*, vol. 112, no. 13, p. 133904, Apr. 2014.

[10] N. Bergeal, F. Schackert, M. Metcalfe, R. Vijay, V. E. Manucharyan, L. Frunzio, D. E. Prober, R. J. Schoelkopf, S. M. Girvin, and M. H. Devoret, "Phase-preserving amplification near the quantum limit with a Josephson ring modulator", *Nature*, vol. 465, no. 7294, pp. 64–68, May 2010.

[11] Y. Zhang, B. J. Lester, Y. Y. Gao, L. Jiang, R. J. Schoelkopf, and S. M. Girvin, "Engineering bilinear mode coupling in circuit QED: Theory and experiment", *Physical Review A*, vol. 99, no. 1, p. 012314, Jan. 2019.

[12] Y. Y. Gao, B. J. Lester, Y. Zhang, C. Wang, S. Rosenblum, L. Frunzio, L. Jiang, S. M. Girvin, and R. J. Schoelkopf, "Programmable Interference between Two Microwave Quantum Memories", *Physical Review X*, vol. 8, no. 2, p. 021073, Jun. 2018.

[13] C. Macklin, K. O'Brien, D. Hover, M. E. Schwartz, V. Bolkhovsky, X. Zhang, W. D. Oliver, and I. Siddiqi, "A near-quantum-limited Josephson traveling-wave parametric amplifier", *Science*, vol. 350, no. 6258, pp. 307–310, 2015.

[14] A. B. Zorin, "Josephson Traveling-Wave Parametric Amplifier with Three-Wave Mixing", *Physical Review Applied*, vol. 6, no. 3, p. 034006, Sep. 2016.

[15] A. B. Zorin, M. Khabipov, J. Dietel, and R. Dolata, "Traveling-Wave Parametric Amplifier Based on Three-Wave Mixing in a Josephson

Metamaterial", in *2017 16th International Superconductive Electronics Conference (ISEC)*, Jun. 2017, pp. 1–3.

[16] A. A. Adamyan, S. E. de Graaf, S. E. Kubatkin, and A. V. Danilov, "Superconducting microwave parametric amplifier based on a quasi-fractal slow propagation line", *Journal of Applied Physics*, vol. 119, no. 8, p. 083901, Feb. 2016.

[17] M. T. Bell and A. Samolov, "Traveling-Wave Parametric Amplifier Based on a Chain of Coupled Asymmetric SQUIDs", *Physical Review Applied*, vol. 4, no. 2, p. 024014, Aug. 2015.

[18] A. Miano and O. A. Mukhanov, "Symmetric Traveling Wave Parametric Amplifier", *IEEE Transactions on Applied Superconductivity*, vol. 29, no. 5, pp. 1–6, Aug. 2019.

[19] A. F. Kockum, V. Macrì, L. Garziano, S. Savasta, and F. Nori, "Frequency conversion in ultrastrong cavity QED", *Scientific Reports*, vol. 7, no. 1, p. 5313, Jul. 2017.

[20] N. E. Frattini, U. Vool, S. Shankar, A. Narla, K. M. Sliwa, and M. H. Devoret, "3-Wave Mixing Josephson Dipole Element", *Applied Physics Letters*, vol. 110, no. 22, p. 222603, Feb. 2017.

[21] N. E. Frattini, V. V. Sivak, A. Lingenfelter, S. Shankar, and M. H. Devoret, "Optimizing the Nonlinearity and Dissipation of a SNAIL Parametric Amplifier for Dynamic Range", *Physical Review Applied*, vol. 10, no. 5, p. 054020, Nov. 2018.

[22] V. Sivak, N. Frattini, V. Joshi, A. Lingenfelter, S. Shankar, and M. Devoret, "Kerr-Free Three-Wave Mixing in Superconducting Quantum Circuits", *Physical Review Applied*, vol. 11, no. 5, p. 054060, May 2019.

[23] M. H. Devoret, A. Wallraff, and J. M. Martinis, "Superconducting Qubits: A Short Review", *arXiv:cond-mat/0411174*, Nov. 2004.

[24] U. Vool and M. Devoret, "Introduction to quantum electromagnetic circuits", *International Journal of Circuit Theory and Applications*, vol. 45, no. 7, pp. 897–934, 2017.

[25] A. Barone and G. Paternò, "Weak Superconductivity — Phenomenological Aspects", in *Physics and Applications of the Josephson Effect*. John Wiley & Sons, Ltd, 1982, pp. 1–24.

[26] B. D. Josephson, "Possible new effects in superconductive tunnelling", *Physics Letters*, vol. 1, no. 7, pp. 251–253, Jul. 1962.

[27] V. Bouchiat, D. Vion, P. Joyez, D. Esteve, and M. H. Devoret, "Quantum coherence with a single Cooper pair", *Physica Scripta*, vol. 1998, no. T76, p. 165, Jan. 1998.

[28] I. Siddiqi, R. Vijay, F. Pierre, C. M. Wilson, M. Metcalfe, C. Rigetti, L. Frunzio, and M. H. Devoret, "RF-Driven Josephson Bifurcation Amplifier for Quantum Measurement", *Physical Review Letters*, vol. 93, no. 20, p. 207002, Nov. 2004.

[29] M. Mirrahimi, Z. Leghtas, V. V. Albert, S. Touzard, R. J. Schoelkopf, L. Jiang, and M. H. Devoret, "Dynamically protected cat-qubits: a new paradigm for universal quantum computation", *New Journal of Physics*, vol. 16, no. 4, p. 045014, Apr. 2014.

[30] R. Boyd, "Nonlinear Optics - 3rd Edition", 2008.

[31] H. Kanter and A. H. Silver, "Self-Pumped Josephson Parametric Amplification", *Applied Physics Letters*, vol. 19, no. 12, pp. 515–517, Dec. 1971.

[32] M. A. Castellanos-Beltran and K. W. Lehnert, "Widely tunable parametric amplifier based on a superconducting quantum interference device array resonator", *Applied Physics Letters*, vol. 91, no. 8, p. 083509, Aug. 2007.

[33] M. A. Castellanos-Beltran, K. D. Irwin, G. C. Hilton, L. R. Vale, and K. W. Lehnert, "Amplification and squeezing of quantum noise with a tunable Josephson metamaterial", *Nature Physics*, vol. 4, no. 12, pp. 929–931, Dec. 2008.

[34] B. Ho Eom, P. K. Day, H. G. LeDuc, and J. Zmuidzinas, "A wideband, low-noise superconducting amplifier with high dynamic range", *Nature Physics*, vol. 8, no. 8, pp. 623–627, Aug. 2012.

[35] A. Ranadive, M. Esposito, L. Planat, E. Bonet, C. Naud, O. Buisson, W. Guichard, and N. Roch, "A reversed Kerr traveling wave parametric amplifier", *arXiv:2101.05815 [cond-mat, physics:quant-ph]*, Feb. 2021.

[36] J. Y. Mutus, T. C. White, E. Jeffrey, D. Sank, R. Barends, J. Bochmann, Y. Chen, Z. Chen, B. Chiaro, A. Dunsworth, J. Kelly, A. Megrant, C. Neill, P. J. J. O'Malley, P. Roushan, A. Vainsencher, J. Wenner, I. Siddiqi, R. Vijay, A. N. Cleland, and J. M. Martinis, "Design and characterization of a lumped element single-ended superconducting microwave parametric amplifier with on-chip flux bias line", *Applied Physics Letters*, vol. 103, no. 12, p. 122602, Sep. 2013.

[37] V. V. Sivak, S. Shankar, G. Liu, J. Aumentado, and M. H. Devoret, "Josephson Array-Mode Parametric Amplifier", *Physical Review Applied*, vol. 13, no. 2, p. 024014, Feb. 2020.

[38] A. Miano and O. A. Mukhanov, "Superconducting traveling-wave parametric amplifier", US Patent US20 200 350 880A1, Nov., 2020.

[39] R. Lescanne, M. Villiers, T. Peronnin, A. Sarlette, M. Delbecq, B. Huard, T. Kontos, M. Mirrahimi, and Z. Leghtas, "Exponential suppression of bit-flips in a qubit encoded in an oscillator", *Nature Physics*, vol. 16, no. 5, pp. 509–513, May 2020.

[40] A. Roy and M. Devoret, "Introduction to parametric amplification of quantum signals with Josephson circuits", *Comptes Rendus Physique*, vol. 17, no. 7, pp. 740–755, Aug. 2016.

[41] J. Niemeyer, "PTB-Mitt. 84, 251 (1974); GJ Dolan", *Appl. Phys. Lett*, vol. 31, p. 337, 1977.

[42] J. Niemeyer and V. Kose, "Observation of large dc supercurrents at nonzero voltages in Josephson tunnel junctions", *Applied Physics Letters*, vol. 29, no. 6, pp. 380–382, Sep. 1976.

[43] S. Probst, F. B. Song, P. A. Bushev, A. V. Ustinov, and M. Weides, "Efficient and robust analysis of complex scattering data under noise in microwave resonators", *Review of Scientific Instruments*, vol. 86, no. 2, p. 024706, Feb. 2015.

[44] J. R. Johansson, P. D. Nation, and F. Nori, "QuTiP: An open-source Python framework for the dynamics of open quantum systems", *Computer Physics Communications*, vol. 183, no. 8, pp. 1760–1772, Aug. 2012.

[45] R. Caruso, D. Massarotti, A. Miano, V. V. Bolginov, A. B. Hamida, L. N. Karelina, I. V. Vernik, V. V. Ryazanov, O. A. Mukhanov, G. P. Pepe, and F. Tafuri, "Ferromagnetic Josephson Junctions for High Performance Computation", *Proceedings*, vol. 12, no. 1, p. 16, Feb. 2019.

[46] R. Caruso, D. Massarotti, A. Miano, V. V. Bolginov, A. B. Hamida, L. N. Karelina, G. Campagnano, I. V. Vernik, F. Tafuri, V. V. Ryazanov, O. A. Mukhanov, and G. P. Pepe, "Properties of Ferromagnetic Josephson Junctions for Memory Applications", *IEEE Transactions on Applied Superconductivity*, vol. 28, no. 7, pp. 1–6, Oct. 2018.

[47] R. Caruso, D. Massarotti, V. V. Bolginov, A. B. Hamida, L. N. Karelina, A. Miano, I. V. Vernik, F. Tafuri, V. V. Ryazanov, O. A. Mukhanov, and G. P. Pepe, "RF assisted switching in magnetic Josephson junctions", *Journal of Applied Physics*, vol. 123, no. 13, p. 133901, Apr. 2018.

[48] L. Parlato, R. Caruso, A. Vettoliere, R. Satariano, H. G. Ahmad, A. Miano, D. Montemurro, D. Salvoni, G. Ausanio, F. Tafuri, G. P. Pepe, D. Massarotti, and C. Granata, "Characterization of scalable Josephson memory element containing a strong ferromagnet", *Journal of Applied Physics*, vol. 127, no. 19, p. 193901, May 2020.

[49] S. Pal and C. Benjamin, "Tuning the 0 - π Josephson junction with a magnetic impurity: Role of tunnel contacts, exchange coupling, e - e interactions and high-spin states", *Scientific Reports*, vol. 8, no. 1, p. 5208, Mar. 2018.

[50] E. C. Gingrich, B. M. Niedzielski, J. A. Glick, Y. Wang, D. L. Miller, R. Loloee, W. P. Pratt Jr, and N. O. Birge, "Controllable 0–π Josephson junctions containing a ferromagnetic spin valve", *Nature Physics*, vol. 12, no. 6, pp. 564–567, Jun. 2016.

[51] M. J. A. Stoutimore, A. N. Rossolenko, V. V. Bolginov, V. A. Oboznov, A. Y. Rusanov, D. S. Baranov, N. Pugach, S. M. Frolov, V. V. Ryazanov, and D. J. Van Harlingen, "Second-Harmonic Current-Phase Relation in Josephson Junctions with Ferromagnetic Barriers", *Physical Review Letters*, vol. 121, no. 17, p. 177702, Oct. 2018.